Monthly Notices
of the
ROYAL ASTRONOMICAL SOCIETY

MNRAS **444,** 3845–3862 (2014) doi:10.1093/mnras/stu1709

Chemodynamics of a simulated disc galaxy: initial mass functions and Type Ia supernova progenitors

C. G. Few,[1,2]★ S. Courty,[3,4,5] B. K. Gibson,[2,6] L. Michel-Dansac[3,4,5] and F. Calura[7]

[1]*School of Physics, University of Exeter, Stocker Road, Exeter EX4 4QL, UK*
[2]*Jeremiah Horrocks Institute, University of Central Lancashire, Preston PR1 2HE, UK*
[3]*Université de Lyon, F-69003 Lyon, France*
[4]*Université Lyon 1, Observatoire de Lyon, 9 avenue Charles André, F-69230 Saint-Genis Laval, France*
[5]*CNRS, UMR 5574, Centre de Recherche Astrophysique de Lyon, Ecole Normale Supérieure de Lyon, F-69007 Lyon, France*
[6]*Institute for Computational Astrophysics, Department of Astronomy and Physics, Saint Mary's University, Halifax, NS B3H 3C3, Canada*
[7]*INAF, Osservatorio Astronomico di Bologna, via Ranzani 1, I-40127 Bologna, Italy*

Accepted 2014 August 17. Received 2014 July 28; in original form 2013 November 18

ABSTRACT

We trace the formation and advection of several elements within a cosmological adaptive mesh refinement simulation of an $L\star$ galaxy. We use nine realizations of the same initial conditions with different stellar initial mass functions (IMFs), mass limits for Type II and Type Ia supernovae (SNII, SNIa) and stellar lifetimes to constrain these subgrid phenomena. Our code includes self-gravity, hydrodynamics, star formation, radiative cooling and feedback from multiple sources within a cosmological framework. Under our assumptions of nucleosynthesis we find that SNII with progenitor masses of up to 100 $M_{\odot}$ are required to match low-metallicity gas oxygen abundances. Tardy SNIa are necessary to reproduce the classical chemical evolution 'knee' in [O/Fe]–[Fe/H]: more prompt SNIa delayed time distributions do not reproduce this feature. Within our framework of hydrodynamical mixing of metals and galaxy mergers we find that chemical evolution is sensitive to the shape of the IMF and that there exists a degeneracy with the mass range of SNII. We look at the abundance plane and present the properties of different regions of the plot, noting the distinct chemical properties of satellites and a series of nested discs that have greater velocity dispersions are more α-rich and metal poor with age.

Key words: methods: numerical – Galaxy: abundances – galaxies: evolution – galaxies: formation.

1 INTRODUCTION

The abundance of different elements is a key astrophysical observable, with variations occurring over a large range of spatial and temporal scales which provide deep insights into the formation and evolution of galaxies. Modelling the chemical evolution of galaxies is an extremely useful tool largely because the differing nucleosynthetic origins of chemical species created in stars tells us a great deal about the large-scale assembly not only of galaxies but also of clusters.

Complex theoretical models of nucleosythesis (Arnett 1978; Iben & Truran 1978; Chiosi & Caimmi 1979; Nomoto, Thielemann & Wheeler 1984; Maeder 1992; Woosley & Weaver 1995; van den Hoek & Groenewegen 1997; Portinari, Chiosi & Bressan 1998; Iwamoto et al. 1999; Marigo 2001; Limongi & Chieffi 2003; Chieffi & Limongi 2004; Izzard et al. 2004; Kobayashi et al. 2006; Karakas & Lattanzio 2007; Doherty et al. 2010; Karakas 2010) tell us how the mass of different stars influences the quantity of different elements that are synthesized during their lifetime and any subsequent supernova (SN) nucleosynthesis that takes place. Through various ejection mechanisms, such as SN mass ejection or stellar winds, these elements are recycled into the interstellar medium (ISM) from which subsequent generations of stars may form. The characteristic abundance ratios of nucleosynthetic sources with different lifetimes result in an evolving chemical signature in the ISM which is imprinted on to stars and may be observed, particularly in long-lived stellar populations (Carbon et al. 1987; Edvardsson et al. 1993; Bensby et al. 2005; Reddy, Lambert & Allende Prieto 2006). Further complications to this framework come in the form of dilution by gas inflow, loss of metal-rich gas through galactic outflows/fountains, galaxy mergers and the internal motion of gas and stars, all of which are rich in detail and complex to model.

Chemical evolution models (CEMs) began as 'seminumerical' approaches with parametrizations of star formation, stellar lifetimes, nucleosynthesis and gas dilution (e.g. Talbot & Arnett 1971;

★ E-mail: c.gareth.few@googlemail.com

Pagel & Patchett 1975; Tinsley 1980; Matteucci & Francois 1989; Carigi 1994; Chiappini, Matteucci & Gratton 1997; Gibson 1997; Ramírez, Allende Prieto & Lambert 2007; Calura et al. 2010). Previous attempts to add a cosmological context to chemical evolution modelling used semi-analytical models set in a Λ cold dark matter (ΛCDM) background (Calura & Menci 2009; Yates et al. 2013). Both seminumerical and semi-analytical approaches are powerful tools for constraining the aspects of input physics considered, but the limitations of these tools are that they do not follow the hydrodynamics of the gas, the advection of metals or easily track physical processes on subgalactic scales. We will show later that features exist in the abundance ratio plane that do not arise without hydrodynamical simulation. The ever increasing capacity of high performance computers to run elaborate simulations has allowed CEMs to be combined with dynamical simulations (Lia, Portinari & Carraro 2002; Kawata & Gibson 2003; Valdarnini 2003; Kobayashi 2004; Tornatore et al. 2004; Romeo, Portinari & Sommer-Larsen 2005; Martínez-Serrano et al. 2008; Oppenheimer & Davé 2008; Wiersma et al. 2009; Shen, Wadsley & Stinson 2010) in what is referred to as 'chemodynamics'. All these models are based upon a Lagrangian approach [smoothed particle hydrodynamics (SPH)] with little or no attention given to Eulerian approaches. In Few et al. (2012a) we sought to remedy this, with the presentation of modifications to the adaptive mesh refinement (AMR) code RAMSES that allowed the chemodynamics to be simulated in an approach that complements existing Lagrangian codes.

The significance of chemodynamics is that while the way that the initial mass function (IMF) and star formation history give rise to chemical evolution is clear, it can also be demonstrated that the chemical evolution indirectly influences the hydrodynamics of the ISM. The radiative cooling rates of plasmas depends upon the chemical composition and has a knock-on effect on metal transport in galaxies (Scannapieco et al. 2005). This non-linear feedback between element production and star formation is linked to the well-known energetic feedback loop between SNe and star formation in dynamical simulations.

In this work we consider the influence of the IMF and Type Ia supernova (SNIa) progenitors. The IMF defines the fraction of stars in each mass interval, controlling the weighting of each nucleosynthetic source and the strength of different energy sources in SN feedback. A qualitative description of the IMF was first formalized by Salpeter (1955) as a description of the 'original mass function' but numerous multislope IMFs (Tinsley 1980; Scalo 1986, 1998; Kroupa, Tout & Gilmore 1993; Kroupa 2001) have now been proposed and present a predicted luminosity function that is much closer to observations. At the present time, separate studies are converging towards a stellar IMF with a log-normal form proposed by Chabrier (2003) which is similar to the multipower law IMF of Kroupa (2001) used in this study.

Our understanding of an important site of nucleosynthesis, SNIa progenitors, is lacking with regard to the lifetime of the progenitors. In this work we do not make any specific assumption concerning the nature of the progenitors by using a parametrization of the timescale of SNIa called the delayed time distribution (DTD) which may be determined empirically. This DTD is the normalized SNIa rate of a simple stellar population (SSP).

The metal enrichment in numerical simulations has been followed in a similar manner to the work presented here for the intergalactic medium/intracluster medium (IGM/ICM; Tornatore et al. 2007, 2010; Wiersma et al. 2009), elliptical galaxies (Kawata & Gibson 2003) and disc galaxies (Kobayashi & Nakasato 2011; Brook et al. 2012b; Agertz et al. 2013; Bekki & Meurer 2013; Martel, Kawata & Ellison 2013). Most of these works employ Lagrangian methods for the numerical hydrodynamics and to date few studies of the influence of the IMF and SNIa formalism has been conducted with grid codes. Conventional treatments of SPH suffer from well-known issues in resolving hydrodynamical instabilities in certain regimes (Agertz et al. 2007; Tasker et al. 2008) and also lack implicit diffusion of metals between local particles. It must be said that great success has been had with the inclusion of turbulent mixing models (Shen et al. 2010), yet the diffusion coefficient associated with this mixing has a strong influence on (for example) the galactic metallicity distribution function (Pilkington et al. 2012b). AMR codes not only provide an essentially natural diffusion via mixing but are also very capable in resolving instabilities (Agertz et al. 2007; Tasker et al. 2008). Other code comparison papers (Frenk et al. 1999; O'Shea et al. 2005; House et al. 2011; Pilkington et al. 2012a; Scannapieco et al. 2012) note the variable results that come from galaxies evolved with different codes.

In this work we use the RAMSES-CH code presented in Few et al. (2012a) to compare multiple realizations of a single galaxy in a cosmological environment that use different subgrid CEMs with the aim of providing constraints on the IMF and SNIa progenitors. We will also demonstrate that the cosmological assembly of a galaxy leaves important signatures within its chemical abundance properties. We vary the IMF over a range of slopes that covers those used in the literature and also change the SNIa scheme to compare three models with different DTDs. Additional models are used to examine the influence of the Type II supernova (SNII) mass range and the binary fraction.

The layout of the paper is as follows. In Section 2 we describe the initial conditions, numerical method and CEMs employed in this work. In Section 3 we demonstrate a kinematic decomposition of the galaxy disc and spheroid, detail the general structural properties of the realizations and present the star formation and SN rate histories, abundance space diagrams and decompose the abundance plane into different formation episodes. Section 4 is a discussion of the results followed by our conclusions in Section 5.

2 METHOD

2.1 Code

In this work we use RAMSES-CH (Few et al. 2012a) a chemodynamical version of RAMSES (Teyssier 2002) to simulate a disc galaxy in a cosmological context with subgrid physics accounting for star formation, SNe and chemical evolution.[1] Dark matter and stars move in the gravitational potential as *N*-body particles while the hydrodynamical evolution is followed by an adaptive grid that automatically increases the resolution for local overdensities. The hydrodynamics grid is used to advect the abundance of elements H, C, N, O, Ne, Mg, Si, Fe and the global metallicity *Z*.

Star particles are permitted to form in gas with a density $n_{\rm g} > n_0$ ($=0.3\,{\rm cm}^{-3}$) and are spawned stochastically (Dubois & Teyssier 2008) at an average rate of $\dot{\rho}_* = \epsilon_* \rho_{\rm g}/t_{\rm ff}$, where $t_{\rm ff} = (3\pi/32 G\rho_{\rm g})^{1/2}$ is the local free-fall time of gas, $\rho_{\rm g}$ is the gas mass density and ϵ_* ($=0.01$) is the star formation efficiency which is constrained such that the simulation can reproduce the Schmidt–Kennicutt relation (Schmidt 1959; Kennicutt 1998).

In each time step star particles eject mass and enrich the surrounding gas as well as injecting energy from SNe. Each star particle has

[1] We are using version 3.07 of RAMSES.

a mass of 8×10^5 M$_\odot$ and represents a SSP. During the SNII phase (∼30 Myr) the most massive stars explode and energy is added to the gas within a sphere that is two grid cells in radius. This energy is added kinetically with a blast wave profile (the velocity of the blast wave is linearly interpolated with radius) that has a total energy of $E_{\rm g,\,K} = \epsilon_{\rm SN} E_{\rm SN} N_{\rm SNII}$, where $N_{\rm SNII}$ is the number of SNII in the star particle exploding in a given time step and $\epsilon_{\rm SN}$ is the efficiency with which the energy per SN ($E_{\rm SN} = 10^{51}$ erg) couples to the surrounding ISM. An efficiency of $\epsilon_{\rm SN} = 1$ is used throughout this work. We find that using $\epsilon_{\rm SN} = 0.5$ leads to an increased stellar mass fraction (of the total mass in the virial radius) from 0.08 to 0.09. As we show later this is not a large change compared to that which arises through changing our CEM but it is somewhat dependent on the other input parameters so greater stellar mass should not be unexpected if choosing a lower value of $\epsilon_{\rm SN}$ than we use here. The superbubble size of two grid cells corresponds to a physical size of 872 pc which is large compared to the true size of superbubbles of ∼100 pc but necessary to implement effective kinetic feedback. The velocity of the blast wave depends upon the mass of the ejecta which may include matter that is swept up, in addition to the mass ejected from stars. This swept up matter is parametrized by $f_{\rm w}$ such that the total mass of gas outflowing from a star particle is $(1 + f_{\rm w})m_{\rm ej}$, where $m_{\rm ej}$ is the mass ejected by the stars themselves. Mass loading the ejecta with this swept up material couples the ISM to feedback more strongly and is necessary to produce galactic outflows. The galactic outflows are necessary for there to be any enrichment of the IGM in our model, however, the downside is that the velocity of the ejected material is diminished as the mass increases such that as the mass-loading factor becomes high enough the feedback becomes unable to effectively remove mass from star formation regions. Having tested several values of $f_{\rm w}$ ranging from 0 to 20 we adopted $f_{\rm w} = 10$ for all models as a compromise that allows IGM enrichment without unduly affecting the ability of feedback to reduce the stellar mass of the galaxy. No more than 25 per cent of a gas cell's mass can be removed by mass loading in order to prevent excessively depleting a gas cell.

Later in the star particle's life it ceases to produce SNII ejections and instead produces SNIa ejections and also asymptotic giant branch (AGB) stellar winds. We will show in Section 2.2 that the number of SNIa is much lower than that of SNII and for this reason we do not employ the same mass/energy injection method for SNIa. This later phase of the star particle's existence is also shared by AGB stellar winds which enrich the local gas. We combine the two sources of mass into a combined AGB/SNIa feedback source, depositing mass and energy (in a thermal form) to the local gas cell only. The energy injected in this situation is simply $E_{\rm g,\,T} = \epsilon_{\rm SN} E_{\rm SN} N_{\rm SNIa}$. We plan to explore the possibility of implementing kinetic feedback for SNIa in future work. While running tests of the code we ran one of our simulations with no SNIa feedback, in this case we found that the stellar mass forming in the halo was slightly higher, but the increase was no larger than the amount we find for differences between our models which are discussed later.

For gas with a high density and low temperature there is a danger that the Jeans length of the gas will be poorly resolved and introduce numerical (and undesirable) fragmentation to the gas. It can be impractical to refine the gas grid sufficiently to provide such resolution in every situation for these simulations. To prevent unphysical fragmentation of the gas we introduce a polytropic equation of state for cool gas ($T < T_{\rm th}$) in the form $T = T_{\rm th}(n_{\rm g}/n_0)^{\gamma - 1}$. At the resolution employed in this work an index of $\gamma = 2$ and a temperature threshold $T_{\rm th} = 2900$ K allows the Jeans length to be resolved by at least four grid cells at all times as advised in Truelove et al. (1997).

Radiative cooling of the gas is computed assuming photoionization equilibrium as a function of temperature for different metallicities and densities. A uniform ultraviolet (UV) background (Haardt & Madau 1996) that has a dependence on redshift provides a heat source. The redshift-dependent contribution to cooling from metals in a photoionized gas is calculated, for temperatures above 10^4 K, via a fit of the difference between the cooling rates at solar metallicity and those at zero metallicity using photoionization code CLOUDY (Ferland et al. 1998). For gas cooler than 10^4 K, metal fine-structure cooling rates are taken from Rosen & Bregman (1995). Note that the polytropic equation of state that is used in these simulations prevents gas from remaining in this low-temperature regime.

2.2 Chemical evolution

The subgrid CEM that RAMSES-CH uses incorporates the IMF, nucleosynthesis models and progenitor lifetimes for each of SNII, SNIa and AGB. These are used to calculate (for different initial metallicities) what the cumulative (as a function of stellar population age) number of SNII, SNIa and AGB is. The table is created in a cumulative form to allow the simulation time step (which is variable) to be completely independent of the feedback table age step; by doing so we need only know the number of, for example, SNII that have exploded in it so far. Using the star particle's age we can look up the number of SNII that should have exploded over its entire lifetime and take the difference to determine how many SNII are due in the current time step. The same method is followed to determine the mass of each element considered and the total ejected mass for each of the nucleosynthetic sources.

2.2.1 Nucleosynthesis yields

We use the nucleosynthetic yields for SNII in Woosley & Weaver (1995) where we adopt the yields associated with the Model B explosion energies for stars with mass greater than 30 M$_\odot$. We have also applied a correction suggested by Timmes, Woosley & Weaver (1995) by halving the Woosley & Weaver (1995) Fe yield. Yields for AGB stars are taken from van den Hoek & Groenewegen (1997). This pair of models is a common choice and when employed in seminumerical models by Romano et al. (2010) were found to reproduce observed Milky Way values of [O/Fe] and [C/Fe] reasonably well, although the same work found that a different combination of yields (Kobayashi et al. 2006; Karakas 2010) performed better overall when considering the majority of elements. Another comparison of nucleosynthesis models was conducted by François et al. (2004) where Woosley & Weaver (1995) yields were found to give the best fits to observations when compared with yields of solar abundance stars from Nomoto et al. (1997) and Limongi & Chieffi (2003); the yields for some elements required modification but in this work we focus upon O and Fe, both of which were found to fit observations well. Stars in the mass range 0.1–8 M$_\odot$ contributed elements in the AGB wind channel and stars from 8 M$_\odot$ up to $m_{\rm SNII,\,u}$ (the upper mass limit on SNII progenitors) are taken as SNII, this upper mass limit is one of the variables in this work. Stars that are more massive than $m_{\rm SNII,\,u}$ are assumed to form but collapse into remnants in the form of black holes and remain in the collisionless stellar particle. Details concerning our input nucleosynthesis can be found in Appendix A.

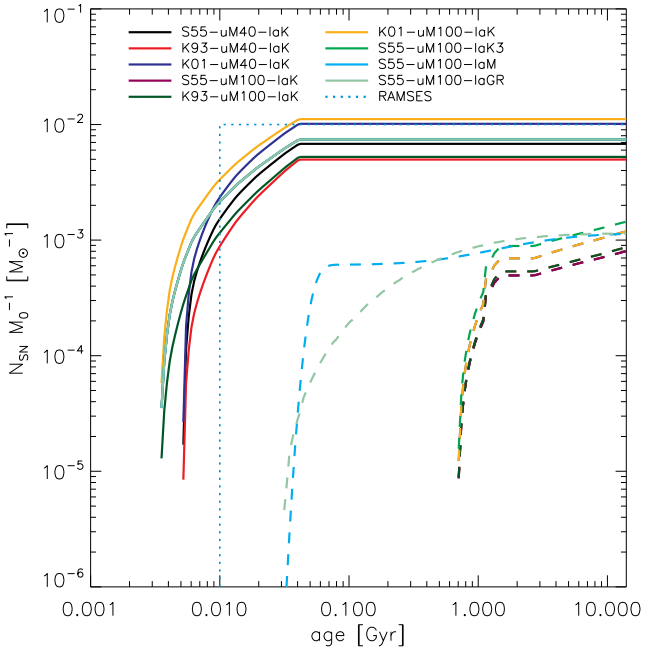

Figure 1. Cumulative SN rates per solar mass formed for a stellar particle (with solar metallicity) for the models tested. Solid lines are the rates of SNII and dashed lines are SNIa, the light blue dotted line is the equivalent SN rate for a standard RAMSES run that parametrizes an S55 IMF, i.e. $\eta_{SN} = 0.1$. The SNII lines of models with the same mass limits ($m_{SNII,l}$ and $m_{SNII,u}$) and IMF overlay one another and are not visible, i.e. models with a name starting âK01-uM40â have the same SNII rates.

2.2.2 *Initial mass functions*

The IMF defines the number of stars that form in a particular mass interval and its shape determines the relative dominance of each nucleosynthetic source. In this work we have selected three IMFs for comparison, which represent the range of slopes that have been proposed by the community. These models are (in ascending order of bias towards stars with masses greater than 8 $M_\odot$), Kroupa et al. (1993), Salpeter (1955) and Kroupa (2001).[2] Henceforth we refer to the Kroupa (2001) IMF as being 'top-heavy' since it is the most biased to massive stars. We have also varied the upper mass limit of SNII progenitors (this does not reflect a change in the IMF merely the lifting of a restriction on progenitor masses) for some models.

The number of SNII in a star particle of initial mass M_0 is calculated by integration over the IMF by number $\phi(m)$ as follows:

$$N_{SNII}(\tau_*, Z_0) = M_0 \int_{MAX(m_{SNII,l}, m_{TO})}^{m_{SNII,u}} \phi(m)\,dm, \quad (1)$$

where m_{TO} is the main-sequence turn-off mass depending on the main-sequence lifetime τ_* and initial metallicity Z_0. This equation is clearly only applicable while $m_{TO}(\tau_*, Z_0)$ is in the sensible range of values for SNII progenitors, $m_{SNII,l}$ (=8 $M_\odot$) to $m_{SNII,u}$. The cumulative SNII rate given by this equation is shown in Fig. 1.

AGB stars are assumed to expel their outer layers in a short period of time (during thermal pulsation) compared with the simulation time step and we calculate the number of AGB stars ejecting their mass in the same way we do for the SNII:

$$N_{AGB}(\tau_*, Z_0) = M_0 \int_{MAX(m_{AGB,l}, m_{TO})}^{m_{AGB,u}} \phi(m)\,dm, \quad (2)$$

while m_{TO} is in the range of AGB masses, $m_{AGB,l}$ to $m_{AGB,u}$ which are 0.5 and 8 $M_\odot$, respectively. To determine turn-off mass as a function of stellar population age we use stellar lifetime models by Kodama & Arimoto (1997) in which the stellar lifetime is a function of both mass and Z_0.

2.2.3 *Type Ia supernovae progenitors*

A different treatment is applied to SNIa; the abundance of elements in the SNIa ejecta is taken as a constant for which we use the yields from Iwamoto et al. (1999) (shown in the right-hand panel of Fig. A1). Three SNIa progenitor models are considered in this work with varying time-scales. The first is taken after Greggio & Renzini (1983) and models C/O WD progenitors, giving them an onset time of ∼30 Myr. In the simulation descriptors of this work, this model is denoted with *IaGR*.

The second SNIa model considered here is by Mannucci, Della Valle & Panagia (2006) and has a more general form with a prompt and a tardy component and is denoted by *IaM* in simulation titles. The *IaGR* and *IaM* models define a time distribution for SNIa but do not explicitly give the number of SNIa until scaled by the number of binary systems that give rise to SNIa explosions. This number is a relatively free parameter but can be chosen such that the present day SNIa rate is reproduced. We have chosen to constrain the number of SNIa to a value that reproduces the SNIa rates measured in the Milky Way when the DTD is applied in a seminumerical scheme (Chiappini et al. 1997; Portinari et al. 1998).

The third model is based on Hachisu, Kato & Nomoto (1999) where the mass range of the SNIa progenitor secondaries is suggested to be bimodal (and is similar to that used in Kobayashi, Tsujimoto & Nomoto 2000 and Kawata & Gibson 2003). In this model, SNIa systems are binaries with a primary mass range of $m_{P,l} = 3\,M_\odot$ to $m_{P,u} = 8\,M_\odot$ which evolves into a C/O WD. Secondaries are either 'main sequence' (MS) or red giant (RG) with mass ranges of $m_{MS,l} = 1.8\,M_\odot$ to $m_{MS,u} = 2.6\,M_\odot$ and $m_{RG,l} = 0.9\,M_\odot$ and $m_{RG,u} = 1.5\,M_\odot$, respectively. The binary fraction for each of the secondary types is $b_{MS} = 0.05$ and $b_{RG} = 0.02$ after Kawata & Gibson (2003). This two-component SNIa model is similar to the Mannucci et al. (2006) model except that the typical mass (and hence time-scale) of the two components are very different; this model has an onset time of 700 Myr. The rate of SNIa in this case is found by a double integration of the IMF and an assumed binary fraction for the two mass ranges:

$$N_{SNIa}(\tau_*) = M_0 \int_{m_{P,u}}^{m_{P,l}} \phi(m)\,dm \times \left[b_{MS} \frac{\int_{MAX(m_{MS,l}, m_{TO})}^{m_{MS,u}} \phi(m)\,dm}{\int_{m_{MS,l}}^{m_{MS,u}} \phi(m)\,dm} + b_{RG} \frac{\int_{MAX(m_{RG,l}, m_{TO})}^{m_{RG,u}} \phi(m)\,dm}{\int_{m_{RG,l}}^{m_{RG,u}} \phi(m)\,dm} \right]. \quad (3)$$

This SNIa model is henceforth denoted by *IaK*; however, note that unlike in the works that inspire this model (Kobayashi et al. 2000; Kawata & Gibson 2003) the IMF for the secondary stars is the same as for the primaries and we have also not applied the metallicity

[2] This IMF is that from Kroupa (2001, p. 234) and not the revised version given later in the paper.

Table 1. CEMs used in the galaxy realizations, see the main text for details. Column (1): Galaxy ID; column (2): initial mass function; column (3): upper mass limit of SNII progenitors; column (4): SNIa progenitor model; columns (5)–(6): binary fractions used in equation (3) for the *IaK* SNIa model.

Realization name	IMF	$m_{\rm SNII,\,u}$ ($M_\odot$)	SNIa DTD	$b_{\rm RG}$	$b_{\rm MS}$
(1)	(2)	(3)	(4)	(5)	(6)
S55-uM40-IaK	S55	40	IaK	0.02	0.05
S55-uM100-IaK	S55	100	IaK	0.02	0.05
K93-uM40-IaK	K93	40	IaK	0.02	0.05
K93-uM100-IaK	K93	100	IaK	0.02	0.05
K01-uM40-IaK	K01	40	IaK	0.02	0.05
K01-uM100-IaK	K01	100	IaK	0.02	0.05
S55-uM100-IaK3	S55	100	IaK	0.036	0.09
S55-uM100-IaM	S55	100	IaM	–	–
S55-uM100-IaGR	S55	100	IaGR	–	–

floor imposed on these objects ([Fe/H] ≥ -1.1) as suggested by Kobayashi et al. (2000). The cumulative SNIa rate for a star particle (that has an instantaneous burst of formation) for these three models is shown in Fig. 1 which illustrates the differing time-scales of each model.

To construct the CEMs used in this work we select an IMF, an upper mass range and an Ia formalism. The naming convention for these combined models starts with either *S55* (Salpeter 1955), *K93* (Kroupa et al. 1993) or *K01* (Kroupa 2001) to denote the IMF, the second part of the name gives the upper mass limit for SNII in $M_\odot$ preceded by '*uM*'. The last part of the name gives the Ia formalism chosen where *IaGR* is Greggio & Renzini (1983), *IaM* is Mannucci et al. (2006) and *IaK* is described in equation (3). We have run models with two different binary fractions for the *IaK* model where one is enhanced to have more SNIa by a factor of 1.8. Table 1 gives an account of the model components and the binary fractions used in the *IaK* models. The chosen binary fractions are well within the limits compiled by Maoz (2008) for the number of stars with masses 3–8 $M_\odot$ that explode as SNIa of 2–40 per cent. Our model *IaK* has 4.7 per cent and *IaK3* has 8.46 per cent, a value similar to the 7 per cent employed in the chemodynamical simulations of Kobayashi & Nakasato (2011). We show two additional models in Appendix B which both employ this enhanced *IaK3* model with a *K01* IMF, these are provided only to demonstrate the effect on another IMF in addition to that used in the main text.

2.3 Simulation framework

The nine chemodynamical simulations that are presented here differ with respect to the CEM they employ but all have the same initial conditions as used in Sánchez-Blázquez et al. (2009) and in Few et al. (2012a) to simulate *K01-uM40-IaK* which is included in this work. The galaxy is taken from a cosmological volume 20 h^{-1} Mpc in size with cosmological parameters as follows: $H_0 = 70\,{\rm km\,s^{-1}}$ Mpc^{-1}, $\Omega_{\rm m} = 0.3$, $\Omega_\Lambda = 0.7$, $\Omega_{\rm b} = 0.042$ and $\sigma_8 = 0.92$. An initial cosmological (with dark matter only) run was performed and a halo with a relatively quiet merger history was selected. This halo was then the subject of a multiresolved simulation with baryons included. Dark matter particles have a mass of 6×10^6 $M_\odot$ in the central region (mass resolution declines further from the box centre to reduce computing time), in comparison a typical stellar particle has a mass of $\sim 8\times 10^5$ $M_\odot$. The physical spatial resolution is 436 pc at grid level = 16. The gas is initiated with a hydrogen content of 75 per cent.

The virial mass of the galaxy halo is approximately 5.6×10^{11} $M_\odot$ and while it exists in a relatively isolated environment it does experience several mergers from small satellite dwarfs.

3 RESULTS

3.1 Kinematic decomposition

To make a fair comparison with observed disc stars we perform a kinematic decomposition to separate halo and bulge stars from the disc star population using the method employed in Abadi et al. (2003), Few et al. (2012b) and Calura et al. (2012). While this method does not completely exclude bulge/halo stars from the disc population, it does significantly reduce contamination by removing those that have kinematic properties clearly inconsistent with the disc.

For each star in the sample the orbital circularity is calculated, i.e. the ratio $J_z/J_{\rm circ}$, where J_z is the angular momentum and $J_{\rm circ}$ is the circular orbit angular momentum for a given particle energy. The distribution is assumed to have a peak at $J_z/J_{\rm circ} = 0$ and at $J_z/J_{\rm circ} = 1$ which correspond to the spheroidal and disc populations, respectively. The spheroidal component of the distribution is assumed to be symmetrical about $J_z/J_{\rm circ} = 0$, particles with negative values of $J_z/J_{\rm circ}$ are designated as spheroid stars. Particles with positive $J_z/J_{\rm circ}$ are attributed to the spheroidal component with a probability proportional to the assumed distribution of spheroid stars. Thus stars are more likely to be designated as part of the spheroid if they are closer to the $J_z/J_{\rm circ} = 0$ peak. All remaining stars are designated 'disc stars'. The disc fraction of each realization is given in Table 2: all are in the range 0.81–0.86.

3.2 Structural properties

The galaxy studied here is a field environment disc galaxy with a virial mass of approximately 5.6×10^{11} $M_\odot$. It experiences several minor mergers and has a small satellite nearby at $z = 0$. The satellite is positioned at a radius of 60 kpc and has a total mass of 7.3×10^9 $M_\odot$.

In Fig. 2 we plot gas density maps (where each pixel represents the mean line-of-sight density) for each of the realizations to show how the subgrid physics affects the shape of the spiral structure. Despite changes to the subgrid model, only slight differences are apparent for most of the realizations. The obvious exception to this is *S55-uM100-IaK3*. This does not stem from changes in the merger history but rather from the additional thermal heating applied to the gas via SNIa feedback which reduces the reservoir of cold gas from which stars may form in the outer regions of the disc. For a comparison of the relative strength of SNIa feedback of the models see Fig. 1. *S55-uM100-IaK3* is smaller than the other discs throughout its history and has the lowest gas fraction of all the realizations, and in keeping with having a smaller disc also has a shorter stellar scale length.

We measure the stellar disc exponential scale length for the galaxies across a radial range between 5 and 15 kpc. This outer edge is in most cases the radius of the break in their Type II density profile (for which an outer disc with a shorter scale length exists), i.e. we measure the scale length of the inner disc and not the outer disc which has a steeper profile. Scale lengths are found to have an average of 3.39 kpc, values for each galaxy can be found in Table 2.

Table 2. Some properties of the galaxies taken at $z = 0$. Column (1): Galaxy ID; column (2): stellar disc scale length; column (3): metallicity gradient of stellar disc; columns (4)–(5): mass fractions calculated within the virial radius; columns (6)–(7): SNII and SNIa rates averaged over the last 3 Gyr for stars within the virial radius, SNuM is the number of SN per 10^{10} $M_{\odot}$ stellar mass; column (8): stellar disc mass fraction (of total stellar mass).

Realization name	Scale length (kpc)	d[Fe/H]/dr (dex kpc^{-1})	Stellar fraction	Gas fraction	SNII rate (SNuM)	SNIa rate (SNuM)	Stellar disc fraction
(1)	(2)	(3)	(4)	(5)	(6)	(7)	(8)
S55-uM40-IaK	3.37	−0.011	0.086	0.063	0.42	0.07	0.81
S55-uM100-IaK	3.49	−0.009	0.088	0.061	0.53	0.07	0.83
K93-uM40-IaK	3.41	−0.011	0.085	0.065	0.36	0.08	0.85
K93-uM100-IaK	3.41	−0.009	0.084	0.066	0.38	0.08	0.86
K01-uM40-IaK	3.64	−0.009	0.078	0.066	0.73	0.12	0.85
K01-uM100-IaK	3.45	−0.009	0.080	0.066	0.97	0.13	0.86
S55-uM100-IaK3	2.95	−0.011	0.094	0.054	0.51	0.14	0.81
S55-uM100-IaM	3.19	−0.008	0.091	0.058	0.41	0.08	0.82
S55-uM100-IaGR	3.58	−0.007	0.087	0.062	0.49	0.08	0.85

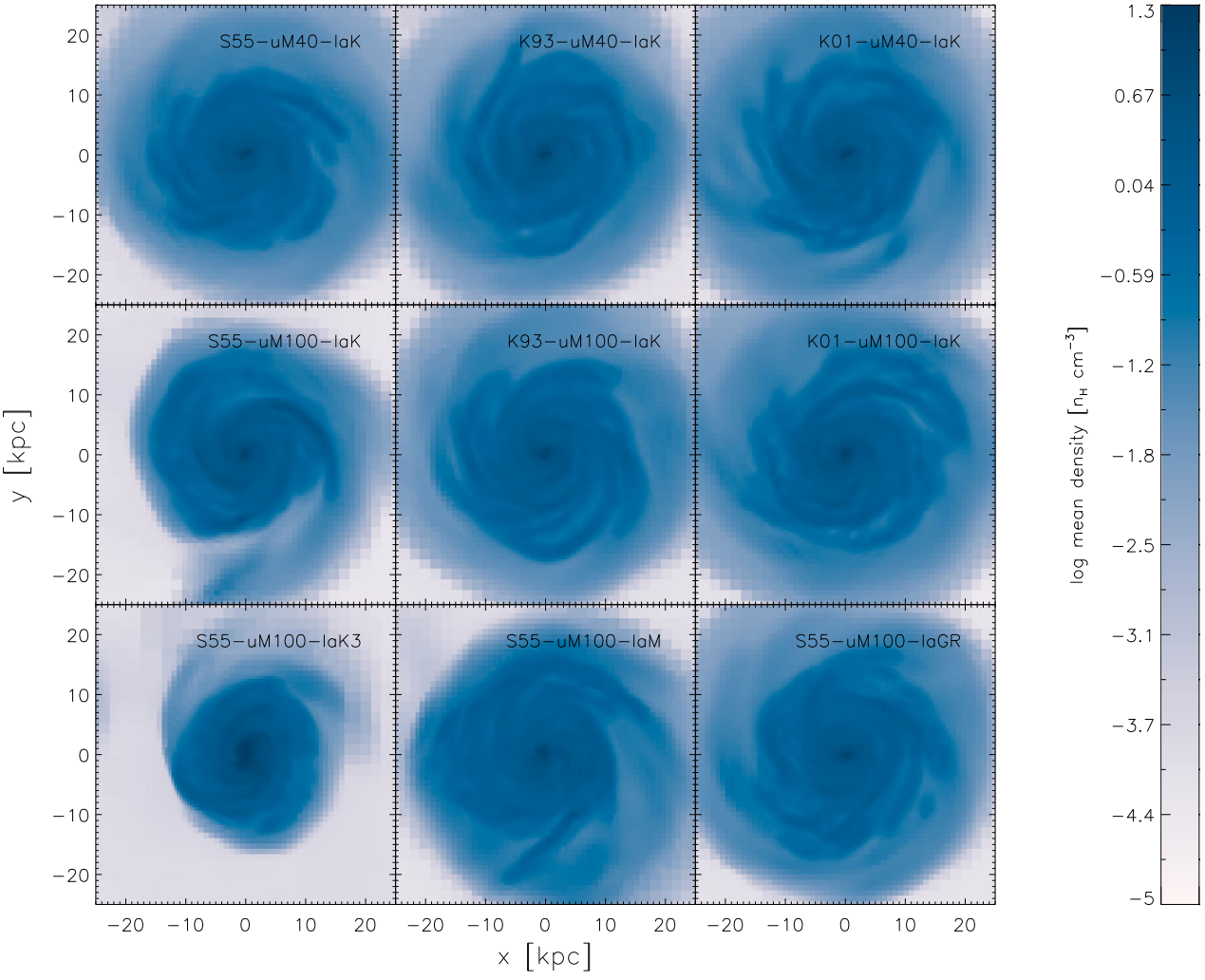

Figure 2. Gas density maps of the simulated galaxies at $z = 0$. Each pixel is coloured by the mean line-of-sight density.

The galaxies have mass-weighted stellar [Fe/H] gradients of $\sim$−0.01 dex kpc^{-1}, consistent with observed gradients in spiral galaxies (Zaritsky, Kennicutt & Huchra 1994). We note that despite these gradients having realistic values they are rather flat which may be symptomatic of the feedback scheme distributing SNII elements over a sphere of radius 872 pc. Another cause of flat metallicity gradients was shown in Pilkington et al. (2012a) where the star formation was shown to be quite uniform with radius which lead very naturally to flat metallicity gradients even before stellar migration. This uniformity of star formation is likely also due to resolution and hence smaller feedback spheres (available at greater resolution) may result in steeper metallicity gradients. The stronger feedback

employed in other simulations has been shown to lead to flatter metallicity gradients (Gibson et al. 2013), particularly at high redshift. Constraints on high-redshift metallicity gradients (Maciel, Costa & Uchida 2003; Yuan et al. 2011; Jones et al. 2013) will reveal whether this is desirable or whether the powerful feedback required by simulations to meet observed properties destroy the high-redshift gradients that we wish to reproduce.

The baryon fraction within the virial radius of the galaxies is not significantly altered by any aspect of the feedback as considered in this work, remaining at ∼15 per cent for most of the realizations. The general robustness of the baryon fraction under the changes to the CEM studied here indicates that the infall rate of gas into the halo for a galaxy of this mass is unaffected by the changes we make to our numerical feedback scheme, which only redistributes baryons within the halo.

While the baryon fraction of the galaxy remains relatively unaffected by changes in the IMF, we do see some small changes in the stellar fraction. The star formation efficiency of the galaxy as a whole is affected by the IMF since different IMFs imply different fractions of gas returned to the ISM; by replenishing the ISM more fuel is available for star formation. The *S55* runs have the most efficient conversion of gas into stars, with stellar mass fraction of *S55-uM100-IaK* at 0.088, this is followed by *K93-uM100-IaK* runs at 0.084, *K01-uM100-IaK* has the lowest stellar fraction at 0.078. Bearing in mind that the *S55* IMF gives rise to a greater number of SNII than does a *K93* IMF this means that increasing the efficiency of the feedback channels in a model does not necessarily result in a reduction in the star formation rate either because it does couple to the ISM in the right way or because the gas available for star formation is replenished by feedback. Guo et al. (2010) calculate the expected stellar mass as a function of halo mass from which we calculate the target stellar mass fraction for the dark matter halo simulated in this work as being 0.035. As expected, the stellar mass is too high, but only by a factor of 2.5.

The disc fraction is measured by taking the fraction of stellar mass that is attributed to the disc by our kinematic decomposition. All the galaxies are disc dominated with the disc accounting for more than 80 per cent of the total stellar mass. The disc fractions of *uM100* runs are consistently higher than those of *uM40* runs by around 1 per cent, this is probably due to the increased level of feedback that redistributes low angular momentum material as suggested by Binney, Gerhard & Silk (2001) and demonstrated in Brook et al. (2011, 2012a).

3.3 Star formation and supernovae rates

In Fig. 3 we show the star formation history and SN rates for each realization of the galaxy among which is the model published previously in Few et al. (2012a), *K01-uM40-IaK*. A spatial cut has been employed in all cases to exclude the nearby satellite with the in-plane distance from the centre limited to 15 kpc and distance from the disc plane limited to 3 kpc. Fig. 3 demonstrates the expected behaviour of SNII rates (in blue) as a function of the underlying IMF. Compare the top two rows of Fig. 3 which have different IMFs with the same upper mass limit (40 $M_\odot$ on the top row and 100 $M_\odot$ on the middle row): the SNII rates are greater in realizations that are more top-heavy (i.e. *K01*). If we now look at the models with different value of $m_{\rm SNII,\,u}$ by comparing models in the top row of Fig. 3 with those immediately below them, increasing $m_{\rm SNII,\,u}$ increases the SNII rate of the galaxy. The IMF has a much weaker effect on the SNIa rate and does not affect the SNIa rate of *IaGR* or *IaM* models at all, in these cases it is due to the fact that the DTD is used independently of the IMF.

The key difference between realizations using differing SNIa models is also as expected, the SNIa rates have slightly different magnitudes but more importantly the onset time of SNIa clearly differs. The appearance of the first SNIa occurs 0.7 Gyr after the first SNII in realizations employing *IaK* SNIa schemes while no offset is visible for those using the *IaGR* and *IaM* schemes. The initial onset of SNIa may not have a strong impact on any but the most metal-poor stars; however, the models with earlier SNIa onset times also create global SNIa rates that have peaks at the same time as the peaks in SNII. This contrasts with the *IaK* scheme that results in SNIa peaks offset from the SNII peaks, a point to which we return later. The final distinction to be made is that the single *S55-uM100-IaK3* realization gives a much greater SNIa rate and in comparison with *S55-uM100-IaK* gives an obviously different star formation history due to the increased thermal feedback. We echo this result by applying the *IaK3* model to a second IMF (*K01*). Because of the larger number of massive stars found with a *K01* compared with a *S55* IMF the enhancement to the SNIa rate is even higher in this case. We show the star formation histories, SN rates and abundance ratio diagrams in Appendix B.

The reader may notice in Fig. 3 that the star formation histories of the realization look broadly similar as one would expect for simulations with the same initial conditions, but that the final peak in star formation (labelled 'd'.) is apparently absent from the panels for *S55-uM100-IaK3* and *S55-uM100-IaM*. These two runs are characterized by low gas fractions compared with the other runs. It is probable perturbing satellites responsible for causing the peaks in star formation are likewise gas poor. Furthermore, the orbits of the satellites are affected by their mass and the mass profile of the host galaxy both of which are different for each realization and will influence how close the perturbing or accreted satellite comes to the disc.

We also compare the quantitative SN rates within the virial radius with those observed by Mannucci et al. (2008) for field Sbc/d galaxies: $0.140^{+0.045}_{-0.035}$ SNuM for SNeIa and $0.652^{+0.164}_{-0.134}$ SNuM for SNeII.[3] We find that most of our SNIa rates are too low, however, models *K01-uM40-IaK*, *K01-uM100-IaK* and *S55-uM100-IaK3* are within the error bars of the Mannucci et al. (2008) observations. SNII rates are consistent with observed values for models *S55-uM100-IaK* and *K01-M40-IaK* while the majority of other models have SNII rates that are too low. Based on the SN rates alone, the most successful model is *K01-uM40-IaK* which is consistent with observed values of both SNeII and SNeIa. This underestimation of the SN rates may at least be partially because they are normalized by stellar mass; the star formation rate of our models at early times is very likely too high which will enhance the stellar mass more than the present day SN rates. Our models also tend to have greater present day star formation rates than observed (a feature common to many numerically simulated galaxies with feedback schemes similar to ours) which would lead to an overestimation of the absolute SNII and SNIa (depending on the promptness of the DTD) rates. The issue of correctly reproducing the star formation history of the galaxy should be addressed before drawing firm conclusions about the IMF based on this kind of analysis.

[3] SNuM units give the number of SN per 10^{10} $M_\odot$ stellar mass.

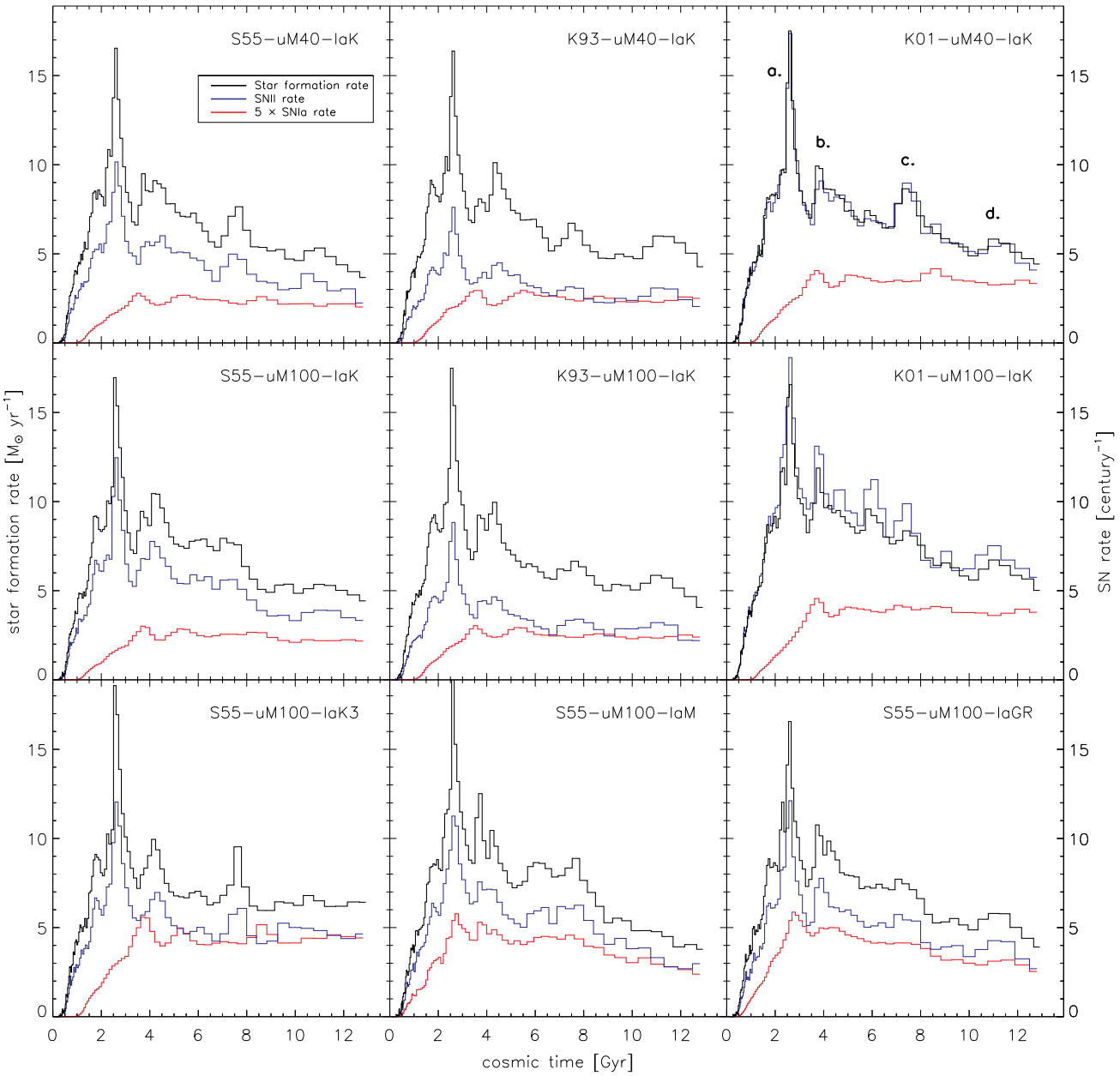

Figure 3. Star formation and SNe rates of each simulation. The black line indicates the star formation rate with the scale given on the left-hand axes. The SN rates are plotted in blue for SNII and red for SNIa. The units are given on the right-hand axes but note that for clarity the SNIa rates are scaled up by a factor of 5. The letters in the upper right-hand panel are used to label the four peaks in star formation for reference in Section 3.5.

3.4 Stellar abundances

Stellar abundance ratios provide a record of the chemical evolution of the galaxy and are regularly used as a constraint on CEMs; the ability of our models to recover this distribution is essential. We now consider the ratios [O/Fe] and [Fe/H] where the square brackets denote that we are taking the logarithm of the mass ratio of the two elements normalized to the solar abundance of those elements. We plot the mass-weighted relative frequency density of stars for these two abundance ratios in Fig. 4. This figure tells us how stars are distributed in the abundance ratio plane, older stars tend to inhabit the low [Fe/H] part of the figure while younger stars are to be found nearer the origin (indicated with dotted lines). Also shown in Fig. 4 are the observations of thin disc, thick disc and halo stars (Gratton et al. 2003; Reddy et al. 2003; Cayrel et al. 2004). Again we note that *K01-uM40-IaK* is the previously published model (Few et al. 2012a). We have renormalized observational data to the same zero-point using the solar abundance measurement of Anders & Grevesse (1989) to allow a consistent comparison to be made between the simulated abundances and the observations that use a variety of solar abundance determinations. As these observations are generally limited to the solar neighbourhood, and in analogy with Calura et al. (2012), we have endeavoured to select stars from the disc at a similar galactocentric radius to the Sun, i.e. 5–11 kpc and with height above (or below) the disc plane of no more than 3 kpc. It should be noted that due to the shallow metallicity gradients of these

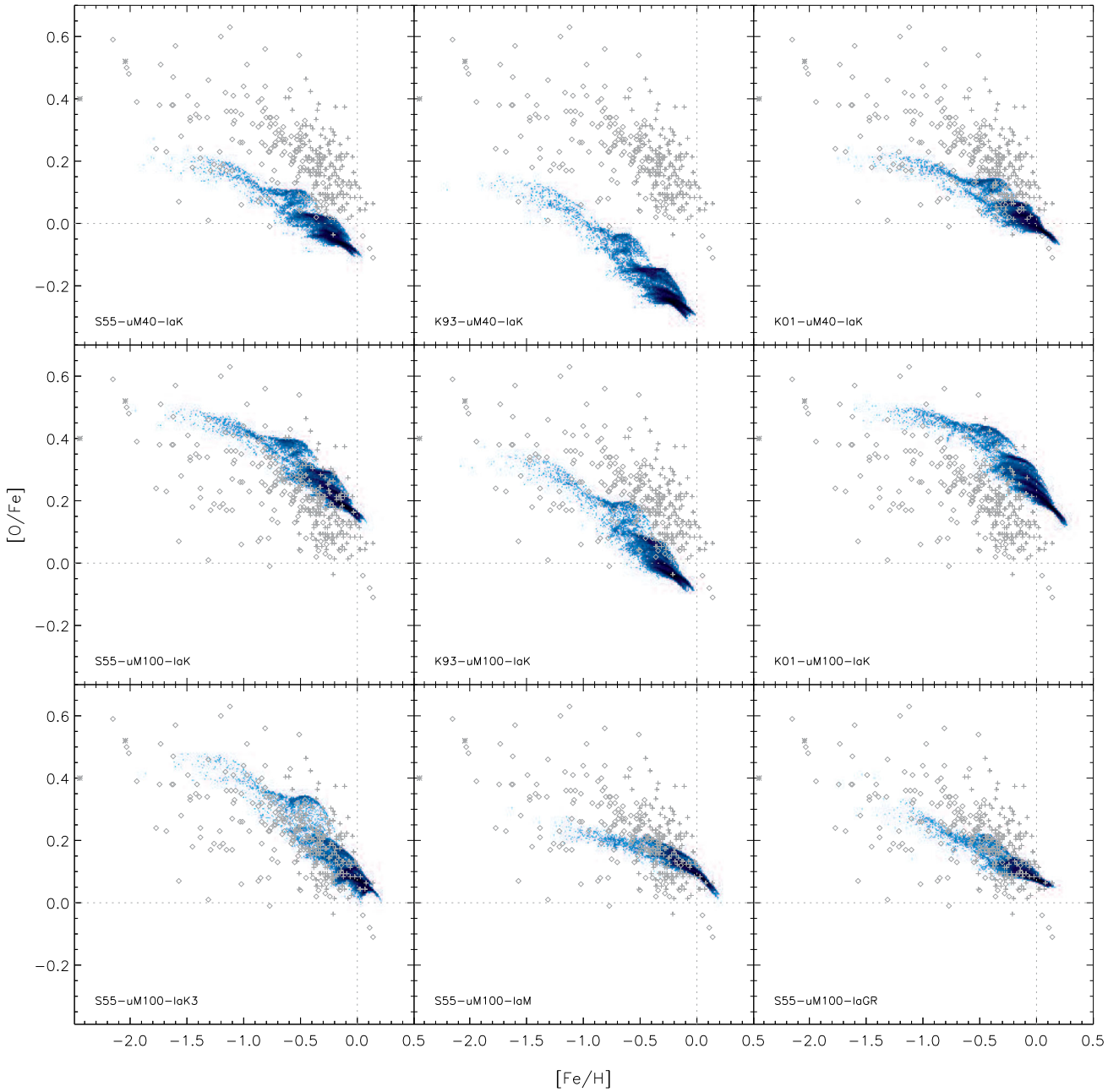

Figure 4. Distribution of 'solar neighbourhood' stars in the abundance plane [O/Fe]–[Fe/H]. Stars are selected from within an annulus of galactocentric radius spanning 5–11 kpc and with height above (or below) the disc plane of no more than 3 kpc and placed in abundance ratio bins weighted by mass. Darker colours indicate a higher relative frequency density. Dotted lines indicate solar abundances. Observations are plotted in grey, diamonds: thick disc and halo stars (Gratton et al. 2003); plus signs: F and G dwarf stars in the thick and thin disc (Reddy et al. 2003) and asterisks: very metal-poor stars (Cayrel et al. 2004).

simulated galaxies the choice of annulus does not affect the results appreciably.

The majority of the models recover the general qualitative trend with an initially high [O/Fe] and a 'knee' at approximately [Fe/H] $= -1$, stars with a great Fe abundance than this have progressively lower [O/Fe]. It can also be seen that the majority of stars have these lower [O/Fe] abundances. Two models do not exhibit this behaviour, *S55-uM100-IaGR* and *S55-uM100-IaM*, and instead have a far smaller dynamic range in [O/Fe] while still extending over the same range in [Fe/H], this is explained further in Section 4.2.

Fig. 4 also demonstrates the strength of the effect of varying the IMF for the simulated galaxies. Models with a top-heavy IMF have a significantly higher O abundance, e.g. models with *K93* have [O/Fe] that is offset lower by ∼0.2 dex compared with their *K01* counterparts. Furthermore the mean [O/Fe] is influenced by changes in $m_{\mathrm{SNII,\,u}}$ with [O/Fe] rising by ∼0.25 dex when we increase $m_{\mathrm{SNII,\,u}}$ from 40 to 100 $\mathrm{M}_{\odot}$. Unlike with changes in the IMF slope, the peak [Fe/H] reached is unaffected due to the very low Fe yield from stars with masses above 40 $\mathrm{M}_{\odot}$.

We calculate the mean [Fe/H] of the solar neighbourhood analogue for each of the realizations (for reference, the maximum

[Fe/H] visible in Fig. 4 is a reasonable proxy) and find a similar trend is seen in the mean value of [Fe/H] with the IMF slope as with [O/Fe]; top-heavy IMFs give higher mean Fe abundances by around 0.2 dex. Altering $m_{\mathrm{SNII,\,u}}$ appears to have less of an impact, again due to the low Fe content in the ejecta of the most massive stars. As expected the enhanced SNIa feedback of *S55-uM100-IaK3* greatly increases the quantity of Fe in the galaxy to a similar value as that models using the top-heavy IMF by Kroupa (2001) and the prompt SNIa models *S55-uM100-IaGR* and *S55-uM100-IaM*. In Appendix we show the effect on the *K01* IMF of introducing the *IaK3* SNIa binary fractions; this leads to a large excess in the Fe content of the galaxy.

It is worth noting features that make this approach different to seminumerical modelling and one such feature is seen at [Fe/H] ≈ -0.5 where [O/Fe] ceases to decline with increasing [Fe/H] for a short time before resuming its decline at slightly greater [Fe/H] to its previous trajectory. Several of these 'knees' appear in all the realizations except for the two that have a low spread in [O/Fe] (*S55-uM100-IaGR* and *S55-uM100-IaM*). These knees are linked to the episodic star formation of the galaxy (which is itself caused by discrete galaxy mergers) and are described further in the next subsection.

Many of the models do not exhibit a great enough dynamic range in [O/Fe] to successfully match the [O/Fe] of both Fe-poor and solar Fe stars. Two of the models *S55-uM100-IaGR* and *S55-uM100-IaM* have already been noted as failing in this respect but even the *IaK* models do not have a steep enough slope to successfully match [O/Fe] across the full range of observations. Only the run with enhanced SNIa numbers (*S55-uM100-IaK3*) has a steep enough slope to successfully match the oxygen abundance across the full range of metallicities.

3.5 Dissecting abundance space

We now examine the chemical element ratio plot for a single galaxy to highlight several interesting features of the abundance plane. In Fig. 5 we bin the stars within the virial radius in one of our realizations (*K01-uM40-IaK*) according to their abundance ratios [O/Fe] and [Fe/H]. Briefly we recall that the schematic behaviour in [O/Fe] versus [Fe/H] for a galaxy with a monotonic star formation history is an initially high [O/Fe] plateau extending from the lowest [Fe/H] up to ≈ -1 followed by a 'knee' at which point the [O/Fe] declines as [Fe/H] increases until both reach the solar value. In our galaxies we see multiple knees preceded by short-lived plateaus that we will refer to as 'strata', these arise from the bursty star formation history.

In the top panel of Fig. 5 the bins are coloured by the relative mass of stars in each bin (as in Fig. 4) to highlight four strata labelled a.–d. which appear to have a limited evolution in [O/Fe] even as [Fe/H] spans a range of approximately 0.3 dex. A fifth feature (e.) has an apparently independent chemical evolution 'stream' with [Fe/H] offset from the majority of other stars by around 0.4 dex (this feature is most clear in the bottom panel of Fig. 5). Henceforth we use the term 'stream' to refer to coherent features in the abundance ratio plane that move diagonally downwards left-to-right in the same fashion as feature e. Parallel to e. is a more metal-rich stream labelled f. the origin of which we describe later.

In the middle panel of Fig. 5 bins are coloured by the mean formation time of the stars therein, indicating that within each of the strata a.–d., the stars have a common formation time. We find that these strata correspond to the four clear peaks in the star formation rate at 2.5, 4.0, 7.5 and 11.0 Gyr seen in Fig. 3 (labelled with the same letters in the upper right-hand panel) during which the SNII rate also increases to temporarily enhance the O content of the galaxy. These successive bursts of star formation thus result in distinctive knees in the top panel of Fig. 5 as the mean [Fe/H] of each strata increases and the mean [O/Fe] decreases since the last episode of star formation. It is worth noting that from the top panel of Fig. 5 it is clear that stratum a. exhibits an up-turn where [O/Fe]

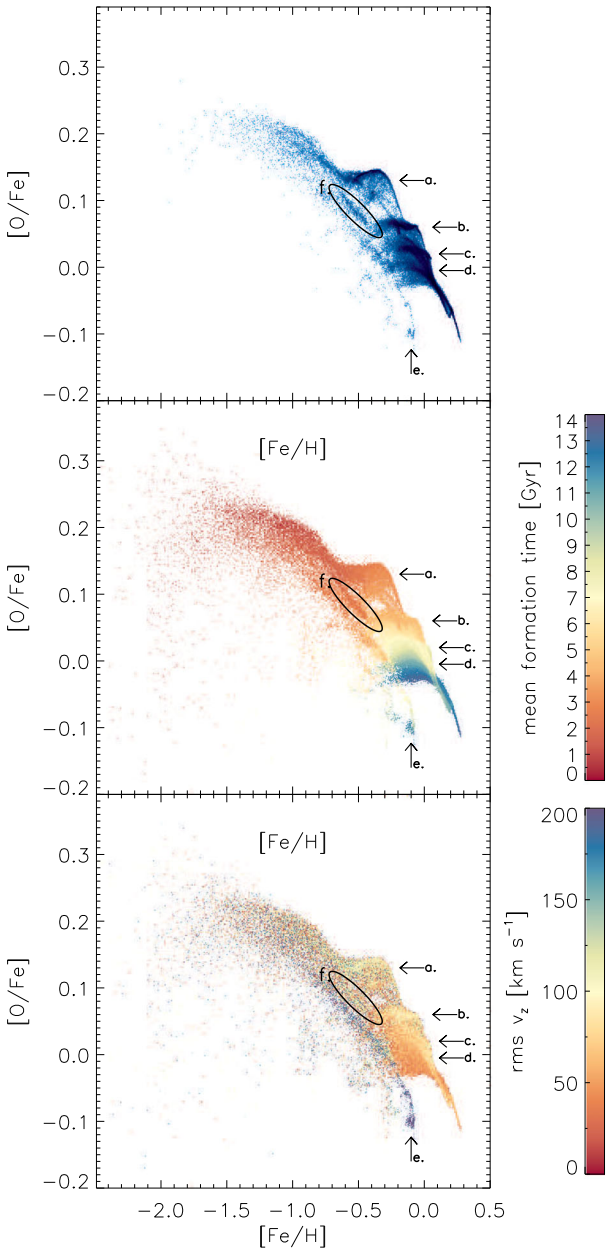

Figure 5. Properties of stars in different regions of the [O/Fe]–[Fe/H] plane for *K01-uM40-IaK*. We bin the stars according to their abundance ratios [O/Fe] and [Fe/H]. In the top panel we colour bins by the relative mass of stars in each bin (as with Fig. 4) to highlight four 'strata' (labelled a.–d.) that are well populated and a fifth feature that has a distinctive low [Fe/H] and [O/Fe]. Darker colour denotes a greater mass. The stars encircled and labelled f. do not form in the galaxy as described more fully in the text. In the middle panel we colour bins by the mass-weighted average formation time of star particles that they contain. In the lower panel we colour bins according to the mass-weighted root-mean-square velocity of the enclosed star particles.

actually increases while b. merely has a constant value in [O/Fe] and c. and d. show increasing ranges of [O/Fe] which is likely due to the strength of the star formation bursts (and thus the associated SNII bursts) diminishing with time (see Fig. 3) and the increasing number of SNIa after the feature with a typical age of 2.5 Gyr. Bear in mind that the rate at which [O/Fe] declines with [Fe/H] will depend upon the number of SNIa; subgrid CEMs with greater SNIa rates will cause these strata to blur into one another.

In the bottom panel of Fig. 5 the bins are coloured according to the root-mean-square vertical velocity (henceforth *velocity dispersion*) of the stars enclosed. In Haywood et al. (2013), solar neighbourhood stars are separated into thin and thick discs based on abundance ratios and age, the thick disc is comparable to the regions labelled as a. and b. here while the thin disc is similar to c. and d. combined. Haywood et al. (2013) give the velocity dispersions of the solar neighbourhood thick and thin disc as 22–50 and 9–35 km s^{-1}, respectively. In another study, Adibekyan et al. (2013) find mean values of 36 and 18 km s^{-1}. These are lower than the typical values of 80–100 km s^{-1} in regions a./b. and 33–40 km s^{-1} in regions c./d. Simulated galaxies are well known as being kinematically hotter due to resolution effects that heat the particle ensemble (e.g. Knebe et al. 2000; House et al. 2011), but we note the trend is qualitatively similar, i.e. the older and more α-rich disc stars have a higher velocity dispersion. The existence of higher velocity dispersion disc stars that are more Fe-poor and α-rich is consistent with a series of older thicker discs, but it must be said that the vertical density profile appears as a continuous transition to longer scale heights rather than a distinct set of scale lengths. The concept of a continuous vertical density distribution that may be interpreted as a thin–thick disc division is explored in Bovy, Rix & Hogg (2012) though here it must be remembered that any simulated thin disc component may be erased due to the resolution. The trends of velocity dispersion and age of stars in different regions in the abundance plane appear to be qualitatively the same as those found by Schönrich & Binney (2009).

We find a picture emerging of a series of superposed disc structures forming with almost discrete ages corresponding to bursts in star formation. The older the disc is the higher its [O/Fe] and the greater its velocity dispersion (and consequently the greater the scale height). This behaviour has been found previously by Bird et al. (2013) (without the context of element abundances) where the youngest stars have velocity dispersions at around 20 km s^{-1}, while older populations have progressively larger velocity dispersions with the oldest populations having dispersions ranging from 60–160 km s^{-1} depending on the galactocentric radius. The trends of velocity dispersion, age and abundance ratios are studied in Minchev, Chiappini & Martig (2013). While the velocity dispersion is again also a function of position, stars with $0.14 < [\mathrm{O/Fe}] < 0.26$ have velocity dispersions of 33–51 km s^{-1} while those with $-0.1 < [\mathrm{O/Fe}] < 0.02$ are lower at 15–43 km s^{-1}. The same qualitative results are shown by Stinson et al. (2013) where the scale height of mono-abundance populations is considered in place of the vertical velocity dispersion: the mono-abundance populations with low [O/Fe] have the shortest scale heights. In each of these works the region of the galaxy considered can have a strong impact on the precise values of velocity dispersion due to radial and vertical trends, however, we see a consistent trend of older disc populations having greater velocity dispersion (i.e. physically thicker) that are also α-rich and Fe-poor compared with the youngest population that reside in a thinner, Fe-rich disc.

The feature e. has a large velocity dispersion and highlights the stars belonging to the nearby satellite at a distance of ∼60 kpc that has a relatively α-poor chemical evolution stream independent of the main galaxy. The satellite may be considered analogous to the Large Magellanic Cloud whose stars are offset to lower [α/Fe] from Milky Way stars (e.g. Johnson, Ivans & Stetson 2006; Lapenna et al. 2012; Van der Swaelmen et al. 2013).

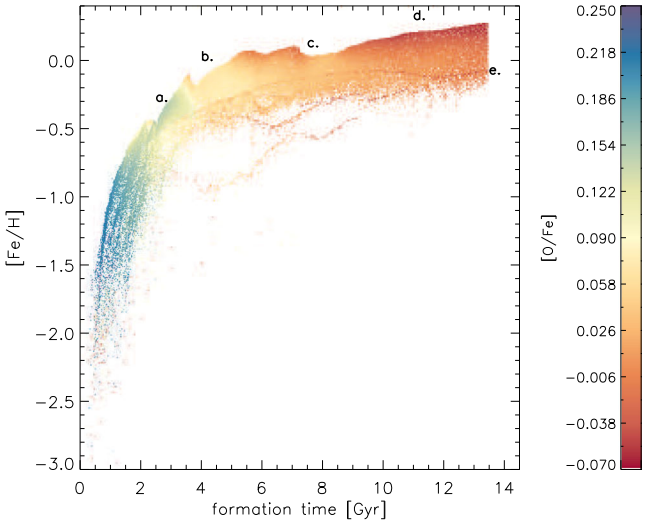

Figure 6. The age–metallicity relation of *K01-uM40-IaK*. Each bin in the figure is coloured according to the [O/Fe] of the stars it contains. We use the labels a.–d. again to note the effect of mergers causing a short-term decline in [Fe/H]. The satellite is also visible in this figure as a thin line of darker red bins against the background of the central galaxy which terminates at label e. The two low-[Fe/H] streams seen in this figure are composed of very few stars and are not attributed to any object in this work.

In addition to the appearance of the satellite as feature e. which has an obviously different position and velocity dispersion there is another stream indicated by an oval (labelled f.) in the top panel of Fig. 5 which is kinematically indistinct from the rest of the galaxy and yet follows an abundance ratio stream parallel to the satellite and does not have the same bumps as the central galaxy. This would suggest that these stars originate in separate objects that have since merged with the central galaxy. We tested this hypothesis by extracting the stars found in this region of the abundance ratio diagram and examining the location of these stars when they formed. This confirmed that the stars originate in several separate structures around the same time as merger activity that resulted in feature a. which later merged with the main galaxy. The extracted stars are not the only ones that formed in independent structures, the oldest stars from the structures in question may also be found mixed with the high-α plateau while the youngest stars from the structures are mixed amongst those of the high-velocity dispersion stars belonging to the satellite.

The age–metallicity diagram for *K01-uM40-IaK* is shown in Fig. 6 with bins that are coloured according to the [O/Fe] of the stars therein. This figure illustrates clearly the temporal evolution of the star-forming gas phase [Fe/H]. We have once again marked the merger times/star formation burst times with the letters a.–d. which shows that the [Fe/H] is briefly diluted before resuming its Fe enrichment. The [O/Fe] of the stars gradually decreases from early times to late with only the most Fe-rich stars extending to subsolar values.

The colour coding in Fig. 6 allows one to see a thin line of relatively [O/Fe] poor stars across the central galaxy terminating at the point marked 'e.' with $[\mathrm{Fe/H}] = -0.1$. This stream corresponds to the satellite stars marked as e. in Fig. 5; however, in Fig. 6 the

satellite stream is not discernable without the benefit of colour coding to separate it from the central galaxy stars. Two new streams are obvious due to their [Fe/H] being much lower than the central galaxy but are composed of very few stars and we do not discuss them further. Earlier we discussed the separation of the stars belonging to feature f. in Fig. 5 from those of the central galaxy, these stars do appear as an independent structure in the age–metallicity diagram. The stars found in feature f. exist in Fig. 6 as coeval with the star formation burst a. at 2.5 Gyr but have similar [Fe/H] and so are not visible as a distinct structure.

4 DISCUSSION

4.1 Oxygen abundance in metal-poor stars

A key constraint on the models exists in the [O/Fe] of metal-poor stars as they are born at a time before SNIa or AGB stars have had time to commence their own enrichment of the ISM, allowing us to examine the effect of SNII enrichment alone. It is clear in Fig. 4 that only the *uM100* models (those with $m_{\mathrm{SNII,\,u}} = 100$ M$_\odot$) are successful in reproducing a high enough value of [O/Fe] for metal-poor stars. If the chosen models is correct this indicates that there is a need for an initial burst of SNII with masses up to 100 M$_\odot$ to produce sufficient oxygen in the model galaxy. This may not however indicate that this upper mass limit is a true representation of that found in nature because of the inherent uncertainty in the abundance of oxygen and iron in high mass stars. As such this result must be viewed in the context of our chosen nucleosynthesis model. This uncertainty is extrapolated for models with $m_{\mathrm{SNII,\,u}} > 40$ M$_\odot$ but should have little impact on our *uM40* models. The qualitative results are consistent with the analytical results in Gibson (1998), i.e. that larger values of $m_{\mathrm{SNII,\,u}}$ generate greater [O/Fe]. Gibson (1998) does however find 40 M$_\odot$ as the minimum value for $m_{\mathrm{SNII,\,u}}$ and notes, as we wish to, that the [O/Fe] plateau does not place tight constraints on $m_{\mathrm{SNII,\,u}}$ due to uncertainties in the yields of massive stars.

Another consideration here is our assumption that all stars more massive than 8 M$_\odot$ end their lives as SNII; hypernovae, SNIb and SNIc may also be important ingredients. Kobayashi & Nakasato (2011) find that as many as 50 per cent of core collapse SNe more massive than 20 M$_\odot$ are required to be the more energetic hypernovae in order to reproduce Zn abundances. This is something we hope to incorporate in future work, particularly since the introduction of hypernovae allows the stellar population to produce stronger feedback energy close to star formation sites with the effect of reducing stellar mass fractions.

One of our main findings is that the mass range of SNII has a strong effect on low-metallicity [O/Fe] values meaning that the poorly constrained yields of stars above 40 M$_\odot$ are of particular interest and future modelling of nucleosynthesis both in massive stars and during the explosive SN phase are extremely valuable.

4.2 Lockstep evolution

We find that the two realizations employing SNIa progenitors models with more prompt DTDs (*S55-uM100-IaGR* and *S55-uM100-IaM*) have a distinctive chemical evolution. SNIa occur much earlier in these models than in models using the more delayed SNIa model *IaK*. This can be seen in Fig. 3 in the initial onset time of SNIa being earlier in these models which gives rise to oxygen-poor low-metallicity stars in comparison with models with the equivalent IMF and $m_{\mathrm{SNII,\,u}}$. Another aspect of this and one that is perhaps more important is that throughout the galaxy's evolution, most of the other models exhibit an offset between peaks in the SNII rate and in the SNIa rate; this is not so for the *S55-uM100-IaGR* and *S55-uM100-IaM* simulations where the SNII and SNIa peaks coincide. This manifests in a 'lockstep' evolution of the abundance ratios shown in Fig. 4 as there is less temporal separation in the elements produced by SNIa (e.g. Fe) and those produced by SNII (e.g. O). This is the reason for the narrow spread and small dynamic range in [O/Fe] in the *IaGR* and *IaM* simulations. Since the characteristic turnover seen at around [Fe/H] $= -1$ seen in other models is due to SNIa becoming relevant sources of enrichment, this feature is not clearly seen in the *S55-uM100-IaGR* and *S55-uM100-IaM* realizations despite the overall slope with [Fe/H].

A channel that produces tardy SNIa is described in Yungelson & Livio (1998) whereby 'edge-lit detonation' occurs in the accreted helium of a C/O WD at sub-Chadrasekhar masses producing a DTD that is similar to that of Kobayashi et al. (1998) but without a gap. The requirement for tardy SNIa to reproduce the knee in the abundance plane has been demonstrated by Kobayashi et al. (1998, 2000) where a double-degenerate SNIa scenario (Tutukov & Yungelson 1994) is compared with the single degenerate model we use in this work (*IaK*) finding that the double-degenerate scenario produced a weak knee, with the single degenerate doing little better. The best model employed the single degenerate DTD with an addition metallicity limit that prevented systems with [Fe/H] < -1.1 from producing SNIa. The metallicity limit is required to represent the effect of the metal content in optically thick winds that transfer mass from the companion to the WD (Hachisu et al. 1999). We find that the existence of a metallicity limit has little effect on the distribution of stars in the abundance plane, but this does not give evidence for or against a metallicity bias in SNIa progenitors. Evidence counter to the concept of metallicity limited SNIa may be found in observed SNIa in low-metallicity environments (Strolger et al. 2002; Quimby et al. 2006; Prieto, Stanek & Beacom 2008) but the existence of multiple SNIa channels may provide an explanation for this inconsistency.

Seminumerical models are used to compare different DTDs in Matteucci et al. (2009), among them that of Matteucci & Recchi (2001) which is very similar to the *IaGR* used in this work, *IaM* and a more tardy model with no prompt component (the first systems explode after 2.5×10^8 yr, with the peak at 3 Gyr) proposed by Strolger et al. (2004).[4] In terms of fitting to observed abundance ratios the two DTDs with prompt components produce abundance ratios falling within observed limits, whereas the tardy Strolger et al. (2004) DTD produces a pronounced knee (perhaps too pronounced) with a plateau at [O/Fe] values above those observed at low metallicity, in each case the models are normalized to solar abundances. In Matteucci & Recchi (2001) there is a clear failure of their *IaGR*-like DTD to reproduce the high-[O/Fe] plateau up to [Fe/H] $= -1$ exhibiting as it does the same gradual decline that we find.

4.3 Type Ia supernova explosion efficiency

It is well known from analytical formulations of chemical evolution that the SNII/SNIa ratio is influenced by the typical time-scale of star formation (e.g. Matteucci & Greggio 1986; Tsujimoto et al. 1995). We note that, as with many simulated galaxies, the star formation rate of the galaxy presented in this work is too high at low redshift. Excessive star formation at late times gives rise to

[4] Note the errata to Strolger et al. (2004).

excessive SNII rates and makes the slope of abundance ratios too shallow above the [Fe/H] ≈ -1 knee and the additional production of α-elements from merger-induced star formation bursts likely worsens the problem. It is clear that the decline in [O/Fe] in the high-metallicity regime is not great enough in the *IaK* models, perhaps due to the poorly reproduced star formation history. In spite of this we wish to demonstrate how the assumed number of SNIa per unit mass of stars formed influences chemical evolution in a numerical context and to do so we increase the fraction of systems giving rise to SNIa in equation (3), factors $b_{\rm RG}$ and $b_{\rm MS}$, by a factor of 1.8 (these models are labelled with *IaK3*).

The enhancement to the SNIa progenitor fraction in the *IaK3* realizations is adequate to steepen the decline in [O/Fe] with increasing [Fe/H] and match the observed slope. We would like to note that enhancements in α-element production may come from the late excess in star formation and also from the exaggerated effect of gas-rich galaxy mergers inducing large bursts in star formation which will result in a slower decline (or even an increase) in [O/Fe] towards higher values of [Fe/H]. This means that in the absence of these systematic effects the models that reproduce the observed distribution in abundance space will be too steep and as such these models should be viewed as representing upper limits to the SNIa progenitor fraction. To simplify the following discussion we borrow the concept of 'explosion efficiency' from Madau, della Valle & Panagia (1998), that is the fraction of stars with masses between 3 and 8 $M_\odot$ that give rise to SNIa. Maoz (2008) compiles numerous estimates of this fraction that range between 2 and 40 per cent. Estimates calculated from abundance ratios tend to be larger at 11–40 per cent (de Plaa et al. 2007; Maoz 2008) as does the value given by Mannucci et al. (2005) from examination of the number of SNIa relative to core collapse SNe in star-forming galaxies (8–15 per cent). In contrast more direct measurements of the SNIa rate per unit star formation rate (e.g. Dahlen et al. 2004; Scannapieco & Bildsten 2005; Sullivan et al. 2006) and per unit mass (e.g. Mannucci et al. 2005, 2008; Sharon et al. 2007) are lower at 0.8–18 per cent. In our *IaK* realizations the fraction is 4.7 per cent while the *IaK3* have 8.46 per cent which is closer to the 7 per cent used for the simulated galaxies in Kobayashi & Nakasato (2011) where a reasonable agreement for many abundance ratios was found with a similar implementation to our SNIa feedback.

While it is beyond the scope of this work, a time varying IMF that steepens with metallicity (e.g. Suda et al. 2013) also has the potential to enhance Fe and reduce O production. Given the controversial nature of variable IMFs we leave this for a more detailed study.

4.4 Abundance strata

We have examined the properties of stars in different regions of the [O/Fe]–[Fe/H] plane to determine how chemical properties may be used to disentangle the origin of those stars. We find that stars may be traced to their formation within independent (prior to accretion by the main galaxy) dark haloes or to individual bursts of star formation induced by mergers.

The decomposition highlights the importance of bursty star formation histories by showing that there are four bands with a narrow spread in [O/Fe] but with a range of [Fe/H]. The ages of stars in these bands are well matched to the time at which the star formation rate increases temporarily during mergers. The rise in star formation creates an enhancement in the number of stars with the particular elemental abundances of the gas at approximately that time. We also see a temporary enhancement in the SNII rate since it closely follows the SFR. The O produced by the SNII during the star formation burst shifts the stars to higher [O/Fe] values, effectively arresting the general trend of declining [O/Fe] with time. We note that similar behaviour will be observed regardless of the cause of the increased star formation rate as in Brook et al. (2012b) where only two abundance strata are seen and are described as an α-rich thick disc and a thin disc population. In this scenario the two strata are delineated by a hiatus in star formation while the [Fe/H] naturally declines; the authors do not attribute the hiatus to any particular event.

We have also examined the vertical velocity dispersion of stars in each region of the abundance plane. We find that the abundance strata at lower [O/Fe] (which are composed of younger stars) have lower velocity dispersions. Since the abundance strata are distinct one might view these as a series of nested disc populations where the [Fe/H] increases, the [O/Fe] decreases and the velocity dispersion (and thus characteristic scale height) increases when comparing older with younger populations. The distinctiveness of the strata depends upon the strength and duration of the relevant star formation bursts, if our simulated star formation histories are more exaggerated than in reality then our strata will be likewise exaggerated. Measuring the variations of star formation rate in real galaxies is difficult but Weisz et al. (2012) find variations that are less than a factor of 10 for galaxies with a comparable mass to our simulated ones. In that context the ratio of the maximum to the accompanying minimums in star formation rate for the galaxies in this work is rather low at $\sim$2.

Within the Milky Way a separation of around 0.2 dex in [O/Fe] of two stellar populations is seen (Bensby et al. 2005; Reddy et al. 2006; Fuhrmann 2008), consistent with our findings for *K01-uM40-IaK* (see Fig. 5). This separation may be a consequence of a hiatus in star formation around 6 Gyr ago that separates the thick disc formation from that of the thin disc. Conversely, Schönrich & Binney (2009) find that even a monotonically decreasing star formation history can produce this kind of bimodality in [O/Fe] through the simple fact that after initially forming an α-rich thick disc, the initial onset of SNIa enrichment forces the [O/Fe] to evolve downward rapidly before settling into a thin disc steady state. A chemically distinct thick disc is also found in simulations by Brook et al. (2012c) and Gibson et al. (2013) where the separation of thick and thin disc in [O/Fe] is 0.1 dex. This is superficially similar to the results presented here except that both of those works find only two offset chemical evolution tracks compared with the three or four seen in our galaxy, this is likely due to the more discrete assembly history of our galaxy.

4.5 Abundance streams

In addition to the abundance strata, we see another feature in the abundance plane that we refer to as 'streams'. The main galaxy stellar abundance simply follows the classical form of a high [O/Fe] plateau followed by a downturn towards higher metallicities. There is also an obviously independent stream offset to lower metallicity (labelled e. in Fig. 5). Only the most metal-rich stars have clear and distinct separation from the main trend but they are more easily separable by age since stars in the stream are older for a given [O/Fe] than those in the central galaxy. This particular stream also has a much higher velocity dispersion than the other galaxy stars. While this stems from the fact that these stars belong to a geographically separate satellite object, we note that the stream would remain recognizable even if this satellite had merged at some time in the past. This satellite might be considered analogous to the Large Magellanic Cloud which follows a chemical evolution that is parallel

but offset from that of the Milky Way (Johnson et al. 2006; Lapenna et al. 2012; Van der Swaelmen et al. 2013).

To strengthen our claim that an accreted site of star formation may be distinguished from the main galaxy using abundance properties we selected stars from another region that remains distinct in the abundance plane (feature f. in Fig. 5) and traced the position of their birth relative to the central galaxy. While there is contamination of this region by stars that formed within the central galaxy, the majority are accreted stars born in several low-mass satellites. The stars are now kinematically and spatially indistinguishable from the galaxy proper but of course retain a distinct chemical evolution.

4.6 Abundance space substructure of other realizations

We have presented an analysis of the substructure of the abundance plane for one of our realizations, *K01-uM40-IaK*. The substructures we have noted also exist in the other simulations presented here. This is clearly seen in Fig. 4, but the substructures are slightly less obvious because this figure contains only stars in the solar neighbourhood whilst Fig. 5 plots all stars in the galaxy. Comparing the panels in Fig. 4, the top and middle rows in particular have qualitatively similar appearance despite variations in the abundance ratios. *S55-uM100-IaK3* also has an obvious second knee, although substructure at lower [O/Fe] is less clear, this is because the CEM gives rise to only three star formation bursts that are more short-lived than in other realizations. As previously discussed, the final two simulations of this galaxy, *S55-uM100-IaM* and *S55-uM100-IaGR*, have a less clear knee due to the prompt onset of SNIa feedback, the slightly less prompt SNIa in *S55-uM100-IaGR* do allow a small second knee to form (the bottom right-hand panel of Fig. 4). This means that knees features are less obvious in chemical space which makes the decomposition described in Section 3.5 more difficult. Decomposition of the chemical properties is not helped by the smaller dynamic range of these realizations as it means the strata overlay one another.

5 CONCLUSIONS

In this work we have implemented additional sources of energetic and nucleosynthetic feedback within the AMR framework of the RAMSES cosmological simulation code. We use the flexibility of the new code to make changes to the subgrid SSP model for resimulations of an $L\star$ disc galaxy. We make changes to the IMF, to the upper mass limit of SNII progenitors and to the DTD of SNIa.

The average scale length of these galaxies is 3.39 kpc and metallicity gradients that, while shallow, are within observed limits. While the range of metallicity gradient reproduced is also narrow compared to observed disc galaxies we do see hints that runs employing SSPs producing a greater number of SNII have flatter gradients. It should be made plain, however, that the flatness of the gradients has much to do with the size of the region over which feedback is distributed (i.e. it may be a resolution issue) as well as the star formation distribution and we are not suggesting that models should make use of less SNII feedback to reproduce steeper metallicity gradients. We also find that the metallicity distribution of the galaxy is narrow compared to observations but with a larger number of stars in the low-metallicity tail as found by Calura et al. (2012) for other simulated galaxies.

All of the runs have quite similar baryon fractions meaning that changes in the feedback strength and metallicity of gas in the halo (of the magnitude produced by our assumptions) do not seem to result in changes to the halo baryon fraction unless these effects contrive to cancel one another. Our variations in the subgrid physics do seem to affect the galaxy formation efficiency with changes in the stellar mass fraction of up to 10 per cent pointing to changes in the way baryons are redistributed by feedback. Since the mass returned to the ISM by the stellar particles depends upon the IMF, and we wish to gauge the efficiency with which a realization forms stars rather than the efficiency with which stellar mass is retained we calculate the 'mass-formed fraction' which is essentially a normalized integration of the star formation history. In this case we note that the realizations with more top-heavy IMFs (those that return more gas to the ISM on shorter time-scales) are more efficient at forming stars even if the stellar mass fraction is not the greatest. We attribute this to the efficient replenishment of the gas reservoir by top-heavy IMFs.

The star formation rate of our simulated galaxies peaks in the first 3 Gyr and subsequent bursts of star formation correspond to mergers. The SNII rate naturally traces the star formation history and increasing the upper mass limit of SNII progenitors naturally leads to increased SNII rates, as does the use of a more top-heavy IMF. The SNIa rate is not strongly dependent on the IMF, but the choice of DTD does make an impact. The only model that satisfactorily reproduces observed SN rates is *K01-uM40-IaK* while all models but one (*S55-uM100-IaK*) are within error bars for the ratio of SNII/SNIa rates. DTDs with a more prompt onset result in SNIa rates that peak close to peaks in the star formation and SNII rates. The prompt onset SNIa DTDs allow a greater amount of Fe enrichment in the first Gyr of evolution. Increasing the number of SNIa in the *IaK3* (compared with the *IaK*) model enhances the amount of thermal feedback and this seems to have a strong impact on the concentration of the galaxy. The additional thermal feedback seems to heat the gas around the disc to a temperature at which it cools efficiently leading to a concentrated disc with a high star formation rate. This is more a function of the thermal mode of feedback employed for SNIa than the efficiency of SNIa themselves and in future studies we will explore a kinetic feedback mode for all channels. The concentration of this galaxy disc has an impact on the galaxy properties, i.e. that it has a shorter scale length and a steeper metallicity gradient. The strongly dissipative mode of formation seen in this realization may be ameliorated with the use of a 'delayed cooling' method as found in Agertz et al. (2013) and implemented in RAMSES by Teyssier et al. (2013).

We see trends in the abundance ratio plane of all galaxies that qualitatively match observed behaviours. Comparing the realizations with one another we see changes in the oxygen and iron abundances that are also as expected: runs with more top-heavy IMFs have greater [O/Fe] values whether caused by the high-mass slope or by the SNII upper mass limit. The reader should note that the nucleosynthesis models we use have a strong impact on our results. The [O/Fe] of low-metallicity stars in particular is defined by the assumed nucleosynthetic processes in massive stars, a regime in which we have to extrapolate the results of Woosley & Weaver (1995) to masses greater than 40 $M_{\odot}$ after halving the iron yields.

Our most tardy SNIa model (*IaK*) is successful at reproducing the turnover at [Fe/H] ≈ -1 but we find that the more prompt SNIa DTDs lead to SNIa rates that peak too soon after star formation and do not allow a relatively SNIa-free phase of enrichment in which the low-metallicity plateau can be established.

The slope of the [O/Fe]–[Fe/H] relation for stars with [Fe/H] $> \approx -1$ is set partly by the star formation history but we find it can be controlled through changes in the binary fraction. The *IaK* models have binary fractions that are too low to match the slope and so we also present a run with a greater number of SNIa per unit stellar mass (*S55-uM100-IaK3*) that successfully reproduces the slope

at high metallicities. The model presented here that uses this enhanced SNIa feedback is coupled with a Salpeter IMF and a SNII upper mass limit of 100 $M_{\odot}$ that reproduces the low-metallicity [O/Fe] plateau: this model is thus our most successful when judged by the abundance ratios alone.

A final note on the constraints placed on the chemical evolution is that our conclusions are based on the star formation history of the galaxy within a simulation. We ask the reader to bear in mind that since our star formation history is excessive at late times compared to the Milky Way, the α-element production is likewise too high meaning that we may not need to invoke such high SNIa binary fractions to match the observed slope in abundance space. Thus we are brought once again to the perennial issue of correctly regulating star formation.

In this work we have used one of our realizations to consider the physical properties of stars in different regions of the abundance ratio plane. We note several features of interest; a succession of strata with lessening [O/Fe] that are produced by consecutive star formation bursts, stars belonging to a satellite that traces a parallel chemical evolution stream offset to lower metallicities and a second parallel stream with a smaller offset but a far smaller range in metallicity. We demonstrate that the strata arise during bursts of star formation and receive enhancements to their [O/Fe] from SNII in stellar particles formed during those bursts. In the final time step of the simulation we find that the younger the abundance strata, the less kinematically hot it is. This leads us to view the strata as chemically identified thick discs, or rather a nested series of ageing and thickening discs.

The satellite retains its individual identity as of the end of the simulation and is more metal poor than the central galaxy. It also does not experience any of the upturns in [O/Fe] as the central galaxy does during mergers. The second stream (that with a smaller offset from the galaxy proper) cannot be easily distinguished geographically or kinematically but when stars in the stream are selected they can be traced back to their birth locations which are in several low-mass accreted bodies.

It is clear that the level of substructure available in abundance space is apt for decomposing the galaxy into the components from which it was assembled. If these structures are indeed realistic and not exaggerated by numerical effects then they are something which is of particular interest in the era of large spectroscopic and kinematic surveys. In future versions of our code we plan to introduce newer nucleosynthesis models that have become available (e.g. Doherty et al. 2010; Pignatari et al. 2013) which cover a greater range of progenitor masses and are more self-consistent with one another. We also hope to include SNIb and SNIc and hypernovae into our CEMs as well as improving on the energetic aspect of stellar feedback.

ACKNOWLEDGEMENTS

CGF thanks Clare Dobbs for suggestions that improved the manuscript and acknowledges the support of the Science and Technology Facilities Council (ST/F007701/1) and funding from the European Research Council for the FP7 ERC starting grant project LOCALSTAR. SC acknowledges support from the BINGO Project (ANR-08-BLAN-0316-01) and the CC-IN2P3 Computing Center (Lyon/Villeurbanne, France), a partnership between CNRS/IN2P3 and CEA/DSM/Irfu. Computing resources were provided by the UK National Cosmology Supercomputer (COSMOS), the University of Central Lancashire's HPC facility and the HPC resources of CINES under the allocation 2012-c2012046642 and 2013-x2013046642 made by GENCI. LM-D acknowledges support from the Lyon Institute of Origins under grant ANR-10-LABX-66. We also thank an anonymous referee for comments which improved the paper.

REFERENCES

Abadi M. G., Navarro J. F., Steinmetz M., Eke V. R., 2003, ApJ, 597, 21
Adibekyan V. Z. et al., 2013, A&A, 554, A44
Agertz O. et al., 2007, MNRAS, 380, 963
Agertz O., Kravtsov A. V., Leitner S. N., Gnedin N. Y., 2013, ApJ, 770, 25
Anders E., Grevesse N., 1989, Geochim. Cosmochim. Acta, 53, 197
Arnett W. D., 1978, ApJ, 219, 1008
Bekki K., Meurer G. R., 2013, ApJ, 765, L22
Bensby T., Feltzing S., Lundström I., Ilyin I., 2005, A&A, 433, 185
Binney J., Gerhard O., Silk J., 2001, MNRAS, 321, 471
Bird J. C., Kazantzidis S., Weinberg D. H., Guedes J., Callegari S., Mayer L., Madau P., 2013, ApJ, 773, 43
Bovy J., Rix H.-W., Hogg D. W., 2012, ApJ, 751, 131
Brook C. B. et al., 2011, MNRAS, 415, 1051
Brook C. B., Stinson G., Gibson B. K., Roškar R., Wadsley J., Quinn T., 2012a, MNRAS, 419, 771
Brook C. B., Stinson G., Gibson B. K., Wadsley J., Quinn T., 2012b, MNRAS, 424, 1275
Brook C. B. et al., 2012c, MNRAS, 426, 690
Calura F., Menci N., 2009, MNRAS, 400, 1347
Calura F., Recchi S., Matteucci F., Kroupa P., 2010, MNRAS, 406, 1985
Calura F. et al., 2012, MNRAS, 427, 1401
Carbon D. F., Barbuy B., Kraft R. P., Friel E. D., Suntzeff N. B., 1987, PASP, 99, 335
Carigi L., 1994, ApJ, 424, 181
Cayrel R. et al., 2004, A&A, 416, 1117
Chabrier G., 2003, ApJ, 586, L133
Chiappini C., Matteucci F., Gratton R., 1997, ApJ, 477, 765
Chieffi A., Limongi M., 2004, ApJ, 608, 405
Chiosi C., Caimmi R., 1979, A&A, 80, 234
Dahlen T. et al., 2004, ApJ, 613, 189
de Plaa J., Werner N., Bleeker J. A. M., Vink J., Kaastra J. S., Méndez M., 2007, A&A, 465, 345
Doherty C. L., Siess L., Lattanzio J. C., Gil-Pons P., 2010, MNRAS, 401, 1453
Dubois Y., Teyssier R., 2008, A&A, 477, 79
Edvardsson B., Andersen J., Gustafsson B., Lambert D. L., Nissen P. E., Tomkin J., 1993, A&AS, 102, 603
Ferland G. J., Korista K. T., Verner D. A., Ferguson J. W., Kingdon J. B., Verner E. M., 1998, PASP, 110, 761
Few C. G., Courty S., Gibson B. K., Kawata D., Calura F., Teyssier R., 2012a, MNRAS, 424, L11
Few C. G., Gibson B. K., Courty S., Michel-Dansac L., Brook C. B., Stinson G. S., 2012b, A&A, 547, A63
François P., Matteucci F., Cayrel R., Spite M., Spite F., Chiappini C., 2004, A&A, 421, 613
Frenk C. S. et al., 1999, ApJ, 525, 554
Gibson B. K., 1997, MNRAS, 290, 471
Gibson B. K., 1998, ApJ, 501, 675
Gibson B. K., Pilkington K., Brook C. B., Stinson G. S., Bailin J., 2013, A&A, 554, A47
Gratton R. G., Carretta E., Claudi R., Lucatello S., Barbieri M., 2003, A&A, 404, 187
Greggio L., Renzini A., 1983, A&A, 118, 217
Guo Q., White S., Li C., Boylan-Kolchin M., 2010, MNRAS, 404, 1111
Haardt F., Madau P., 1996, ApJ, 461, 20
Hachisu I., Kato M., Nomoto K., 1999, ApJ, 522, 487
Haywood M., Di Matteo P., Lehnert M. D., Katz D., Gómez A., 2013, A&A, 560, A109
House E. L. et al., 2011, MNRAS, 415, 2652
Iben I., Jr, Truran J. W., 1978, ApJ, 220, 980

Iwamoto K., Brachwitz F., Nomoto K., Kishimoto N., Umeda H., Hix W. R., Thielemann F., 1999, ApJS, 125, 439
Izzard R. G., Tout C. A., Karakas A. I., Pols O. R., 2004, MNRAS, 350, 407
Johnson J. A., Ivans I. I., Stetson P. B., 2006, ApJ, 640, 801
Jones T., Ellis R. S., Richard J., Jullo E., 2013, ApJ, 765, 48
Karakas A. I., 2010, MNRAS, 403, 1413
Karakas A., Lattanzio J. C., 2007, Publ. Astron. Soc. Aust., 24, 103
Kawata D., Gibson B. K., 2003, MNRAS, 340, 908
Kennicutt R. C., Jr, 1998, ApJ, 498, 541
Knebe A., Kravtsov A. V., Gottlöber S., Klypin A. A., 2000, MNRAS, 317, 630
Kobayashi C., 2004, MNRAS, 347, 740
Kobayashi C., Nakasato N., 2011, ApJ, 729, 16
Kobayashi C., Tsujimoto T., Nomoto K., Hachisu I., Kato M., 1998, ApJ, 503, L155
Kobayashi C., Tsujimoto T., Nomoto K., 2000, ApJ, 539, 26
Kobayashi C., Umeda H., Nomoto K., Tominaga N., Ohkubo T., 2006, ApJ, 653, 1145
Kodama T., Arimoto N., 1997, A&A, 320, 41
Kroupa P., 2001, MNRAS, 322, 231
Kroupa P., Tout C. A., Gilmore G., 1993, MNRAS, 262, 545
Lapenna E., Mucciarelli A., Origlia L., Ferraro F. R., 2012, ApJ, 761, 33
Lia C., Portinari L., Carraro G., 2002, MNRAS, 330, 821
Limongi M., Chieffi A., 2003, ApJ, 592, 404
Maciel W. J., Costa R. D. D., Uchida M. M. M., 2003, A&A, 397, 667
Madau P., della Valle M., Panagia N., 1998, MNRAS, 297, L17
Maeder A., 1992, A&A, 264, 105
Mannucci F., Della Valle M., Panagia N., Cappellaro E., Cresci G., Maiolino R., Petrosian A., Turatto M., 2005, A&A, 433, 807
Mannucci F., Della Valle M., Panagia N., 2006, MNRAS, 370, 773
Mannucci F., Maoz D., Sharon K., Botticella M. T., Della Valle M., Gal-Yam A., Panagia N., 2008, MNRAS, 383, 1121
Maoz D., 2008, MNRAS, 384, 267
Marigo P., 2001, A&A, 370, 194
Martel H., Kawata D., Ellison S. L., 2013, MNRAS, 431, 2560
Martínez-Serrano F. J., Serna A., Domínguez-Tenreiro R., Mollá M., 2008, MNRAS, 388, 39
Matteucci F., Francois P., 1989, MNRAS, 239, 885
Matteucci F., Greggio L., 1986, A&A, 154, 279
Matteucci F., Recchi S., 2001, ApJ, 558, 351
Matteucci F., Spitoni E., Recchi S., Valiante R., 2009, A&A, 501, 531
Minchev I., Chiappini C., Martig M., 2013, A&A, 558, A9
Nomoto K., Thielemann F.-K., Wheeler J. C., 1984, ApJ, 279, L23
Nomoto K., Hashimoto M., Tsujimoto T., Thielemann F.-K., Kishimoto N., Kubo Y., Nakasato N., 1997, Nucl. Phys. A, 616, 79
Oppenheimer B. D., Davé R., 2008, MNRAS, 387, 577
O'Shea B. W., Nagamine K., Springel V., Hernquist L., Norman M. L., 2005, ApJS, 160, 1
Pagel B. E. J., Patchett B. E., 1975, MNRAS, 172, 13
Pignatari M. et al., 2013, ApJS, preprint (arXiv:1307.6961)
Pilkington K. et al., 2012a, A&A, 540, A56
Pilkington K. et al., 2012b, MNRAS, 425, 969
Portinari L., Chiosi C., Bressan A., 1998, A&A, 334, 505
Prieto J. L., Stanek K. Z., Beacom J. F., 2008, ApJ, 673, 999
Quimby R., Höflich P., Kannappan S. J., Rykoff E., Rujopakarn W., Akerlof C. W., Gerardy C. L., Wheeler J. C., 2006, ApJ, 636, 400
Ramírez I., Allende Prieto C., Lambert D. L., 2007, A&A, 465, 271
Reddy B. E., Tomkin J., Lambert D. L., Allende Prieto C., 2003, MNRAS, 340, 304
Reddy B. E., Lambert D. L., Allende Prieto C., 2006, MNRAS, 367, 1329
Romano D., Karakas A. I., Tosi M., Matteucci F., 2010, A&A, 522, A32
Romeo A. D., Portinari L., Sommer-Larsen J., 2005, MNRAS, 361, 983
Rosen A., Bregman J. N., 1995, ApJ, 440, 634
Salpeter E. E., 1955, ApJ, 121, 161
Sánchez-Blázquez P., Courty S., Gibson B. K., Brook C. B., 2009, MNRAS, 398, 591
Scalo J. M., 1986, Fundamentals Cosmic Phys., 11, 1
Scalo J., 1998, in Gilmore G., Howell D., eds, ASP Conf. Ser. Vol. 142, The Stellar Initial Mass Function (38th Herstmonceux Conference). Astron. Soc. Pac., San Francisco, p. 201
Scannapieco E., Bildsten L., 2005, ApJ, 629, L85
Scannapieco C., Tissera P. B., White S. D. M., Springel V., 2005, MNRAS, 364, 552
Scannapieco C. et al., 2012, MNRAS, 423, 1726
Schmidt M., 1959, ApJ, 129, 243
Schönrich R., Binney J., 2009, MNRAS, 399, 1145
Sharon K., Gal-Yam A., Maoz D., Filippenko A. V., Guhathakurta P., 2007, ApJ, 660, 1165
Shen S., Wadsley J., Stinson G., 2010, MNRAS, 407, 1581
Stinson G. S. et al., 2013, MNRAS, 436, 625
Strolger L.-G. et al., 2002, AJ, 124, 2905
Strolger L.-G. et al., 2004, ApJ, 613, 200
Suda T. et al., 2013, MNRAS, 432, L46
Sullivan M. et al., 2006, ApJ, 648, 868
Talbot R. J., Jr, Arnett W. D., 1971, ApJ, 170, 409
Tasker E. J., Brunino R., Mitchell N. L., Michielsen D., Hopton S., Pearce F. R., Bryan G. L., Theuns T., 2008, MNRAS, 390, 1267
Teyssier R., 2002, A&A, 385, 337
Teyssier R., Pontzen A., Dubois Y., Read J. I., 2013, MNRAS, 429, 3068
Timmes F. X., Woosley S. E., Weaver T. A., 1995, ApJS, 98, 617
Tinsley B. M., 1980, Fundamentals Cosmic Phys., 5, 287
Tornatore L., Borgani S., Matteucci F., Recchi S., Tozzi P., 2004, MNRAS, 349, L19
Tornatore L., Borgani S., Dolag K., Matteucci F., 2007, MNRAS, 382, 1050
Tornatore L., Borgani S., Viel M., Springel V., 2010, MNRAS, 402, 1911
Truelove J. K., Klein R. I., McKee C. F., Holliman J. H., II, Howell L. H., Greenough J. A., 1997, ApJ, 489, L179
Tsujimoto T., Nomoto K., Yoshii Y., Hashimoto M., Yanagida S., Thielemann F.-K., 1995, MNRAS, 277, 945
Tutukov A. V., Yungelson L. R., 1994, MNRAS, 268, 871
Valdarnini R., 2003, MNRAS, 339, 1117
van den Hoek L. B., Groenewegen M. A. T., 1997, A&AS, 123, 305
Van der Swaelmen M., Hill V., Primas F., Cole A. A., 2013, A&A, 560, A44
Weisz D. R. et al., 2012, ApJ, 744, 44
Wiersma R. P. C., Schaye J., Theuns T., Dalla Vecchia C., Tornatore L., 2009, MNRAS, 399, 574
Woosley S. E., Weaver T. A., 1995, ApJS, 101, 181
Yates R. M., Henriques B., Thomas P. A., Kauffmann G., Johansson J., White S. D. M., 2013, MNRAS, 435, 3500
Yuan T.-T., Kewley L. J., Swinbank A. M., Richard J., Livermore R. C., 2011, ApJ, 732, L14
Yungelson L., Livio M., 1998, ApJ, 497, 168
Zaritsky D., Kennicutt R. C., Jr, Huchra J. P., 1994, ApJ, 420, 87

APPENDIX A: CHEMICAL EVOLUTION MODEL INPUTS

In this work we employ the nucleosynthesis models of van den Hoek & Groenewegen (1997) for AGB stars, Woosley & Weaver (1995) for SNII and Iwamoto et al. (1999) for SNIa. The mass of different elements ejected from these sources is shown in Fig. A1 as a function of the progenitor mass for stars with an initially solar metallicity. The AGB yield from van den Hoek & Groenewegen (1997) span a range of progenitor mass of 0.8–8 $M_{\odot}$, while model grid from Woosley & Weaver (1995) extends from a maximum of 40 $M_{\odot}$ down to 12 $M_{\odot}$ for most metallicities. To make use of these nucleosynthesis models we interpolate between neighbouring grid points within those models. A void exists between the mass ranges covered by the respective models. When necessary we extrapolate in mass by retaining the fractional abundance of each element and scaling with the mass of the progenitor. These extrapolations are illustrated in Fig. A1 with dot–dashed lines.

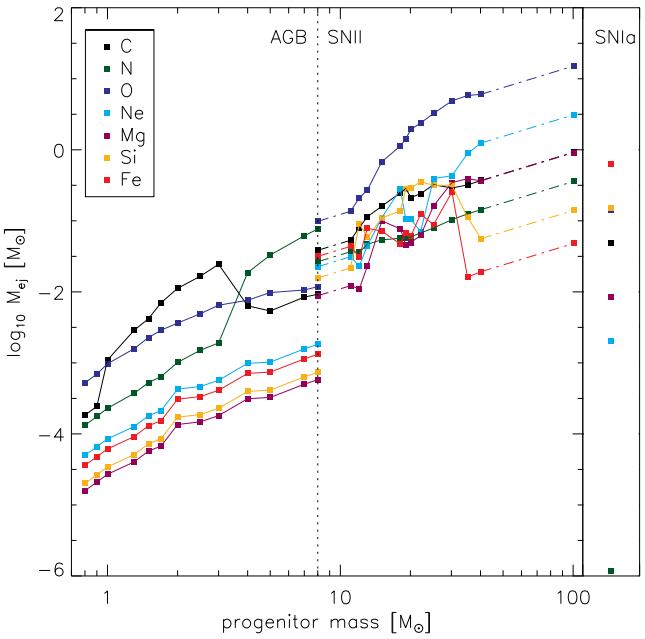

Figure A1. Mass of elements ejected by stars as a function of initial mass. In the right-hand panel we show the abundances for a single SNIa for comparison, no labels are shown on the lower axis for SNIa as the ejecta elements are the same for all SNIa. The mass above which stars are considered to be SNeII progenitors is indicated at 8 $M_{\odot}$ with a dotted line. Data for AGB stars are taken from van den Hoek & Groenewegen (1997), SNeII from Woosley & Weaver (1995), and SNIa from Iwamoto et al. (1999). Points connected by solid lines denote the original data, those connected by dot–dashed lines show adopted. Extrapolations are linear and scaled to the mass of the progenitor star.

The results of this work are clearly dependent on how we handle the yields in the uncertain mass regimes, particularly regarding the most massive stars. In the current version of our model we neglect fallback in massive stars and hypernovae instead simply retaining the same abundance ratios as 40 $M_{\odot}$ stars have. We note that this extrapolation has no impact on our *uM40* models for which all fallback is prevented for stars that are more massive.

In our model we assume stars more massive than 8 $M_{\odot}$ explode as SNII, the yields of the least massive SNII are obtain by assuming the same yield as the least massive SNII in Woosley & Weaver (1995) but scaling down with the progenitors mass. In truth this is probably an overestimation of the yields of these stars but this mass range represents only 1.4–2.5 per cent of the mass of stars formed so it should not have a large impact.

No extrapolation is required to lower masses as the least massive star that ejects mass within the Hubble time is greater than 0.8 $M_{\odot}$ and thus within the mass bounds of the van den Hoek & Groenewegen (1997) models.

APPENDIX B: SUPPLEMENTARY GALAXIES

We performed several additional simulations that are not required in the main text to explain the trends observed. To present our results it was only necessary to show how the SNIa model *IaK3* affected a single IMF, for which we chose *S55*. We now also demonstrate the effect of enhanced SNIa feedback on the *K01* IMF. First we show the *K01-uM100-IaK* model from our main results again alongside a realization where we changed the SNIa model to the enhanced version (*IaK3*), we label this new realization *K01-uM100-IaK3*. A second model is the same in most respects but is subject to a reduced SNII upper mass limit of $m_{\mathrm{SNII,\,u}} = 80\,M_{\odot}$ which is labelled as *K01-uM80-IaK3*.

The star formation and SNe rates of these three realizations are shown in Fig. B1. As is the case with the *S55-uM100-IaK3*, *K01-uM100-IaK3* has a much higher SNIa rate than its *IaK* counterpart and the top-heavy nature of the *K01* IMF makes the impact even stronger which may be responsible for the reduced star formation rate after 8 Gyr. The second new model (*k01-uM80-IaK3*) occupies the right-hand panel in Fig. B1 and has a similar SNIa rate as the previous model, in this case the reduction in both SNII and SNIa feedback resulting from the lower $m_{\mathrm{SNII,\,u}}$ allows the star formation rate to remain slightly higher.

We also show how the abundance ratio plane (shown in Fig. B2) is affected by the introduction of enhanced SNIa chemical feedback. The *K01* models are affected in much the same way as the *S55* models are: the increased SNIa feedback steepens the slope in the high-metallicity regime. When looking at the SN rates in Fig. B1 we noted that since the *K01* IMF is more top-heavy than *S55* the impact is stronger. This is again apparent in Fig. B2 as the Fe content of the galaxy is much higher. While the [O/Fe] ratio is nicely reproduced in this way the [Fe/H] values are too much high, something which is not seen in any of our other models. The excessive production of Fe is somewhat ameliorated in *K01-uM80-IaK3* since both SNII and SNIa rates of stellar particles are reduced.

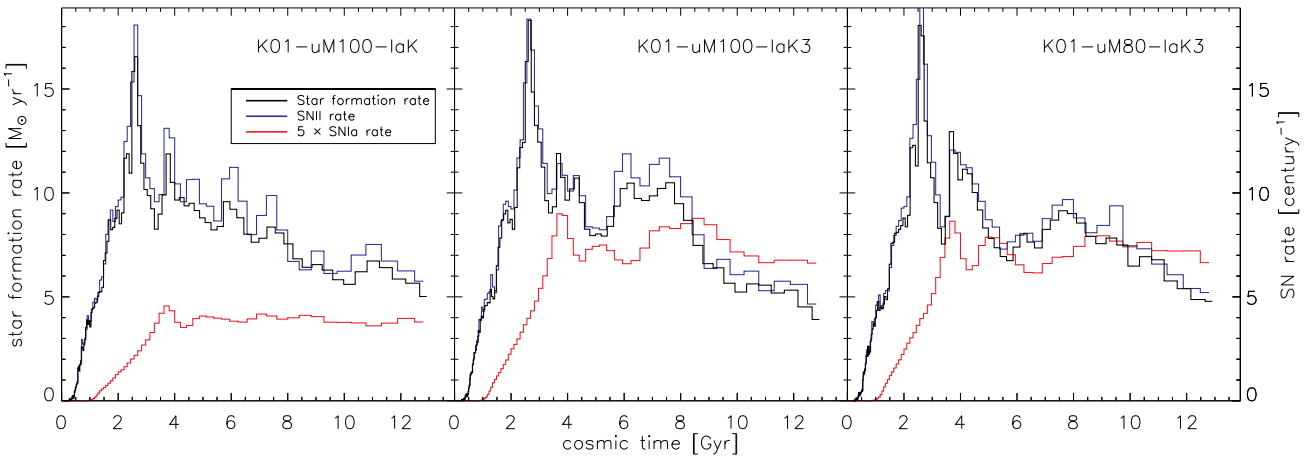

Figure B1. The same as Fig. 3 but for three realizations not discussed in the main text. The black line indicates the star formation rate with the scale given on the left-hand axes. The SN rates are plotted in blue for SNII and red for SNIa. The units are given on the right-hand axes but note that for clarity the SNIa rates are scaled up by a factor of 5.

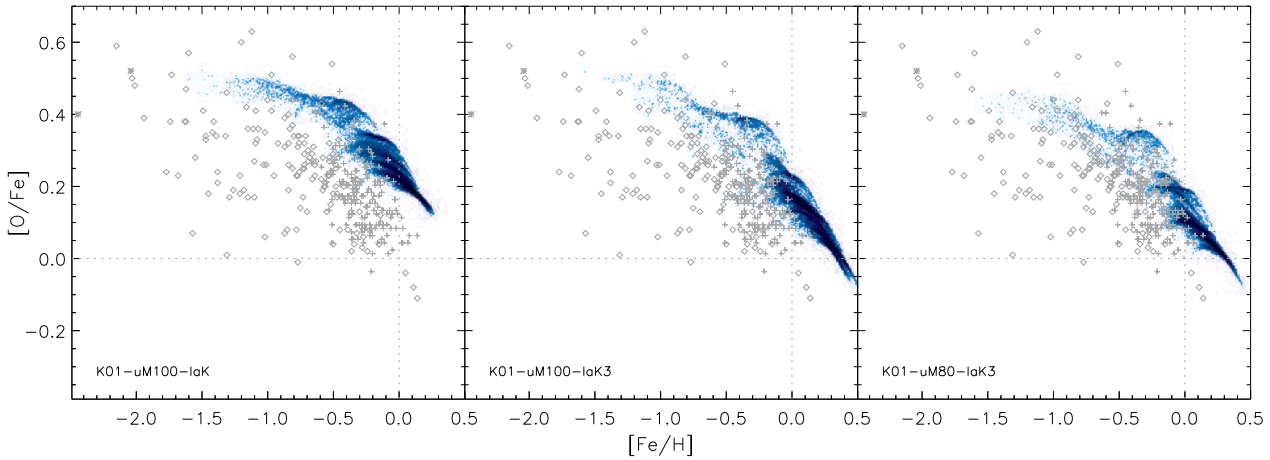

Figure B2. The same as Fig. 4 but for three realizations not discussed in the main text. Darker colours indicate higher relative frequency density. Dotted lines indicate solar abundances. Observations are plotted in grey, diamonds: thick disc and halo stars (Gratton et al. 2003); plus signs: F and G dwarf stars in the thick and thin disc (Reddy et al. 2003) and asterisks: very metal-poor stars (Cayrel et al. 2004).

This paper has been typeset from a TEX/LATEX file prepared by the author.